JM PAPERS

Similarity for dissipation-scaled wall turbulence

S.L. Tang[1],† **and R.A. Antonia**[2]

[1]Center for Turbulence Control, Harbin Institute of Technology, Shenzhen 518055, PR China

[2]School of Engineering, University of Newcastle, NSW 2308, Australia

In this paper, we put forward a hypothesis for turbulent kinetic energy, Reynolds stresses and scalar variance in wall-bounded turbulent flows, whereby these quantities, when normalized with the kinematic viscosity, mean turbulent energy dissipation rate and scalar dissipation rate, are independent of the Reynolds and Péclet numbers when they are sufficiently large. In particular, there exist two scaling ranges: (i) an inertial-convective range at sufficiently large distance from the wall over which a 2/3 power-law scaling emerges for all quantities mentioned above; (ii) a viscous-convective range between the viscous-diffusive and inertial-convective ranges at large Prandtl number over which the normalized scalar variance is constant. The relatively large amount of available wall turbulence data either provides reasonably good support for this hypothesis or at least exhibits a trend that is consistent with the predictions of this hypothesis. The relationship between the proposed scaling and the traditional wall scaling is discussed. Possible ultimate statistical states of wall turbulence are also proposed.

Key words: turbulence theory

1. Introduction

Wall turbulence is ubiquitous both in nature and in many industrial processes. Not surprisingly, its scaling has received significant attention in the literature. The classical view of wall turbulence is that the velocity and passive scalar statistics, such as the mean velocity and mean scalar, Reynolds stresses and scalar (temperature) variance, are universal, depending only on distance from the wall when scaled with the wall parameters u_τ, θ_τ and ν, where $u_\tau = (\tau_w/\rho)^{1/2}$ is the friction velocity (with τ_w the wall shear stress, and ρ the density of the fluid), ν is the kinematic viscosity, and $\theta_\tau = Q_w/\rho c_p u_\tau$ is the friction temperature (with Q_w the averaged wall heat flux, and c_p the specific

† Email address for correspondence: shunlin.tang88@gmail.com

heat at constant pressure). It is widely accepted by the turbulence research community that the scaling of the mean velocity and mean scalar based on wall parameters near the wall is tenable (e.g. Townsend 1976; Monty *et al.* 2009; Marusic *et al.* 2010; Smits, McKeon & Marusic 2011*b*; Vincenti *et al.* 2013; Lee & Moser 2015; Willert *et al.* 2017; Alcántara-Ávila, Hoyas & Pérez-Quiles 2021; Pirozzoli *et al.* 2021, 2022; Hoyas *et al.* 2022). However, several decades of research into wall turbulence have shown that the wall scaling of quantities such as the Reynolds stresses and scalar (temperature) variance is untenable in the near-wall region, at least at finite Reynolds numbers (e.g. Marusic *et al.* 2010; Smits *et al.* 2011*b*; Vincenti *et al.* 2013; Lee & Moser 2015; Willert *et al.* 2017; Samie *et al.* 2018; Alcántara-Ávila *et al.* 2021; Pirozzoli *et al.* 2021, 2022; Hoyas *et al.* 2022). In particular, the available evidence shows that the peak values of the streamwise Reynolds stress $\overline{u_1 u_1}^+$ (hereafter $\overline{u_1 u_1}_p^+$) and the scalar variance $\overline{\theta\theta}^+$ (hereafter $\overline{\theta\theta}_p^+$) increase systematically with Re_τ for the former (see, for example, Marusic, Baars & Hutchins (2017) and references therein) where the maximum value of Re_τ is approximately 20 000, and for the latter (see, for example, figure 11(*b*) of Pirozzoli *et al.* 2022) where the maximum value of Re_τ is approximately 6000. The Kármán number Re_τ can be interpreted as the ratio of the outer length scale δ, i.e. the boundary layer thickness, pipe radius or channel half-width, to the viscous length scale ν/u_τ; the streamwise (x_1), wall-normal (x_2) and spanwise (x_3) velocity fluctuations are denoted respectively by u_1, u_2 and u_3; γ is the thermal diffusivity; θ denotes the scalar fluctuation; the overbar denotes an averaged value at a given x_2 location with respect to the homogeneous spatial directions and time; + denotes normalization by u_τ, θ_τ and ν. More specifically, with few exceptions (Hultmark *et al.* 2012; Vallikivi, Hultmark & Smits 2015*b*) where the data near $x_2^+ \approx 15$ may have been affected by insufficient spatial resolution (Marusic *et al.* 2017), there appears to be strong support for the argument that $\overline{u_1 u_1}_p^+$ and $\overline{\theta\theta}_p^+$ grow logarithmically (e.g. Marusic *et al.* 2017; Pirozzoli *et al.* 2022). It is worth mentioning that the logarithmic growth implies that $\overline{u_1 u_1}_p^+ \sim \overline{\theta\theta}_p^+ \to \infty$ as $Re_\tau \to \infty$, suggesting the failure of wall scaling. In contrast, in a recent paper, Chen & Sreenivasan (2021) reasoned that the bounded dissipation rate for $\overline{u_1 u_1}^+$ at the wall (which has yet to be observed) leads to a finite $\overline{u_1 u_1}_p^+$ at infinite Reynolds number, suggesting a recovery of wall scaling. In particular, they proposed an alternative formula for the dependence of $\overline{u_1 u_1}_p^+$ on Re_τ, which, like the logarithmic growth, provides a plausible description for the behaviour of $\overline{u_1 u_1}_p^+$ in pipe and channel flows, and the boundary layer at finite Reynolds numbers. Smits *et al.* (2021) showed that the Reynolds stresses, after normalization by the variance of the wall shear stress fluctuation (or equivalently, the dissipation rate for $\overline{u_1 u_1}^+$ at the wall), collapse reasonably well in the near-wall region. Note also that Antonia & Kim (1994) had previously observed that a normalization based on Kolmogorov velocity and length scales, defined at the wall, is more appropriate in the wall region than scaling on τ_w and ν. We emphasize that the use of the dissipation rate for $\overline{u_1 u_1}^+$ at the wall for normalization is equivalent to the use of the mean turbulent energy dissipation rate $\bar\varepsilon$ ($\equiv \nu \overline{(\partial u_i/\partial x_k)(\partial u_i/\partial x_k)}$) at the wall when their ratio is independent of the flow type; this behaviour was observed by Tang & Antonia (2022) in a channel and a boundary layer for $Re_\tau > 1000$. Some interesting issues arise.

(i) Are $\bar\varepsilon$, ν and the mean scalar dissipation rate $\bar\varepsilon_\theta$ ($\equiv \gamma \overline{(\partial\theta/\partial x_k)(\partial\theta/\partial x_k)}$) (or equivalently, the Batchelor–Kolmogorov scales $\theta_B = (\bar\varepsilon_\theta(\nu/\bar\varepsilon)^{1/2})^{1/2}$, $u_K = (\nu\bar\varepsilon)^{1/4}$ and $\eta = (\nu^3/\bar\varepsilon)^{1/4}$) the proper scaling parameters for $\overline{u_i u_j}$ (and also the turbulent kinetic energy $\overline{u_i u_i}$) and $\overline{\theta\theta}$?

(ii) What is the relationship between the scaling parameters $\bar{\varepsilon}$, ν and $\bar{\varepsilon}_\theta$, and the conventional wall parameters (u_τ, θ_τ and ν) in the context of $\overline{u_i u_j}$, $\overline{u_i u_i}$ and $\overline{\theta\theta}$?

(iii) Tang & Antonia (2022) proposed a hypothesis for small-scale wall turbulence whereby small-scale statistics, when normalized by the Batchelor–Kolmogorov scales, are independent of the flow type as well as of the Reynolds and and Péclet numbers. It seems therefore natural to enquire into the relationship between the scaling of small-scale wall turbulence and that of statistics associated with $\overline{u_i u_j}$, $\overline{u_i u_i}$ and $\overline{\theta\theta}$. The major objective of this paper is to address these issues.

2. A hypothesis for $\overline{u_i u_j}$, $\overline{u_i u_i}$ and $\overline{\theta\theta}$

The transport equations for the turbulent kinetic energy $\overline{u_i u_i}$ and the scalar variance $\overline{\theta\theta}$ in a channel are given by (e.g. Pope 2000; Abe, Antonia & Kawamura 2009; Alcántara-Ávila *et al.* 2021)

$$\underbrace{-\overline{u_1 u_2}\frac{\partial \bar{U}_1}{\partial x_2}}_{P_U} \underbrace{-\frac{1}{2}\frac{\partial \overline{u_i^2 u_2}}{\partial x_2}}_{T} \underbrace{-\frac{1}{2}\frac{\partial \overline{u_2 p}}{\partial x_2}}_{P} + \underbrace{\frac{\nu}{2}\frac{\partial^2 \overline{u_i u_i}}{\partial x_2^2}}_{D_\nu} \underbrace{-\bar{\varepsilon}}_{D} = 0, \tag{2.1}$$

$$\underbrace{-\overline{\theta u_2}\frac{\partial \Theta}{\partial x_2}}_{P_\Theta} \underbrace{-\frac{1}{2}\frac{\partial \overline{\theta^2 u_2}}{\partial x_2}}_{T_\theta} + \underbrace{\frac{\gamma}{2}\frac{\partial^2 \overline{\theta^2}}{\partial x_2^2}}_{D_\gamma} \underbrace{-\bar{\varepsilon}_\theta}_{D_\theta} = 0, \tag{2.2}$$

where $\bar{U}_1$ is the mean velocity in the streamwise (x_1) direction, and Θ is the mean scalar. In (2.1), the terms P_U, T, P, D_ν and D are the production, turbulent diffusion, pressure diffusion, molecular diffusion and dissipation rate, respectively. Similarly, in (2.2), terms P_Θ, T_θ, D_γ and D_θ are the production, turbulent diffusion, molecular diffusion and dissipation, respectively. Except for the pressure term (P) in (2.1), which is negligible near the wall and in the outer flow region, the two equations are analogous. This analogy has been tested extensively (e.g. Fulachier & Dumas 1976; Fulachier & Antonia 1984; Antonia, Abe & Kawamura 2009) in both wall and free shear flows.

All terms in (2.1) and (2.2), after normalizing by wall parameters, are shown in figure 1(*a,b*), respectively. Close to the wall, both $\bar{\varepsilon}$ and $\bar{\varepsilon}_\theta$ are approximately balanced by the molecular diffusion. In particular, $\bar{\varepsilon}_\theta$ is very nearly equal to $(\gamma/2)(\partial^2 \overline{\theta^2}/\partial x_2^2)$ in the region $x_2^+ \lesssim 2$ at $Re_\tau = 500\text{–}5000$ and $Pr = \nu/\gamma = 0.71$ (figure 1*b*). However, $\bar{\varepsilon}$ is approximately equal to $(\nu/2)(\partial^2 \overline{u_i u_i}/\partial x_2^2)$ only in the region $x_2^+ \lesssim 0.3$ at $Re_\tau = 550\text{–}10^4$ (figure 1*a*). The pressure diffusion term (P) slowly increases away from the wall up to a maximum value near $x_2^+ \approx 2$, and the magnitude of the ratio of this term to $\bar{\varepsilon}$ is 2.7 % at $x_2^+ \approx 0.3$ and $Re_\tau = 10^4$. Therefore, in these near wall regions, (2.1) and (2.2) reduce to

$$\bar{\varepsilon}^+ = \frac{1}{2}\frac{\partial^2 \overline{u_i u_i}^+}{\partial x_2^{+2}}, \quad \bar{\varepsilon}_\theta^+ = \frac{1}{2 Pr}\frac{\partial^2 \overline{\theta\theta}^+}{\partial x_2^{+2}}, \tag{2.3a,b}$$

when the conventional scaling is used. It is evident that both sides of these two equations depend on Re_τ. However, after normalizing (2.3*a,b*) by $\bar{\varepsilon}$, $\bar{\varepsilon}_\theta$ and ν, we obtain

$$\frac{\partial^2 \overline{u_i u_i}^*}{\partial x_2^{*2}} = 2, \quad \frac{\partial^2 \overline{\theta\theta}^*}{\partial x_2^{*2}} = 2 Pr, \tag{2.4a,b}$$
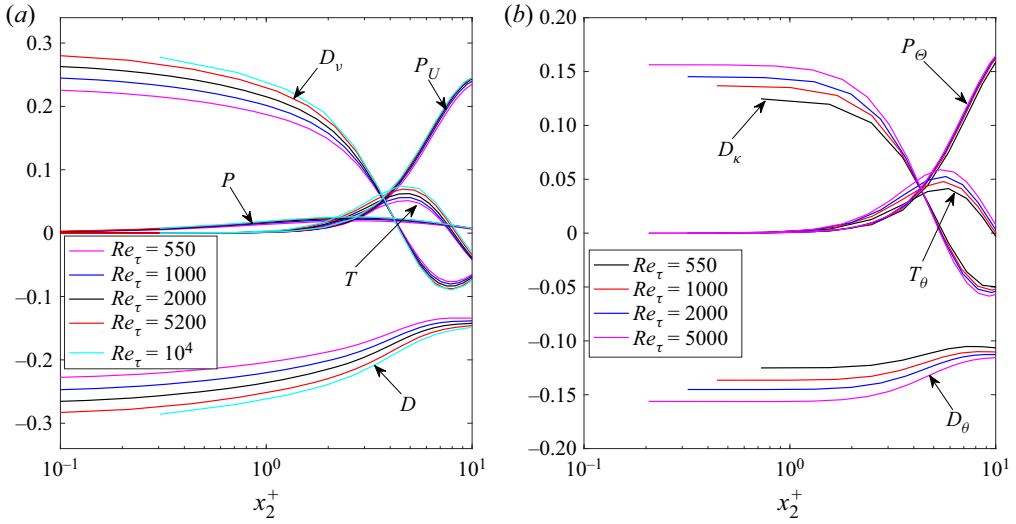
Figure 1. Distributions of terms in (*a*) (2.1) and (*b*) (2.2), normalized by wall parameters, in a channel at $Pr = 0.71$. Data of Lee & Moser (2015, 2019), Alcántara-Ávila *et al.* (2021) and Hoyas *et al.* (2022).

independently of Re_τ. Equations (2.3*a,b*) and (2.4*a,b*) indicate that the scaling based on $\bar{\varepsilon}$, $\bar{\varepsilon}_\theta$ and ν is superior to that based on wall parameters. A similar analysis, based on the transport equations for $\overline{u_i u_i}$ in the range $40 \leq x_2^+ \leq 200$, leads to the same conclusion; see Appendix B. Note that $\bar{\varepsilon}^+$ and $\bar{\varepsilon}_\theta^+$ do not collapse and their magnitudes are large near the wall (figure 1); they arise because of the presence of the wall and, concomitantly, the presence of the mean shear. Therefore, it seems natural to use the local $\bar{\varepsilon}$ and $\bar{\varepsilon}_\theta$, instead of u_τ and θ_τ, to describe the wall turbulence statistics; whilst u_τ and θ_τ are local (wall) quantities, they also balance the momentum flux and heat flux, respectively, across the flow. On the other hand, $\bar{\varepsilon}$ and $\bar{\varepsilon}_\theta$ are quantities that are important in describing the dynamics at every location in the flow via (2.1) and (2.2). For example, $\bar{\varepsilon}$ and $\bar{\varepsilon}_\theta$ are approximately balanced by the molecular diffusion as $x_2^+ \to 0$, while they are approximately balanced by the production and turbulent diffusion at $x_2^+ = 5$ (figure 1). The relationship between the present scaling and the wall scaling will be discussed in some detail in § 4.

Equations (2.4*a,b*) further indicate that the possible scaling parameters for $\overline{u_i u_i}$ and $\overline{\theta\theta}$ are $\bar{\varepsilon}$, $\bar{\varepsilon}_\theta$ and ν; since γ at any equation can be written as $\gamma \equiv \nu/Pr$ (see, for example, (2.4*a,b*)), for simplicity, we consider only $\bar{\varepsilon}$, $\bar{\varepsilon}_\theta$ and ν as the scaling parameters. In this situation, the distance from the wall should be normalized as

$$x_2^* = \frac{x_2}{\eta} = \frac{x_2 u_K}{\nu}, \tag{2.5}$$

where x_2^* is a local Reynolds number so that its magnitude can be expected to determine the relative importance of viscous effects. A more general definition of the local turbulent Reynolds number is

$$Re_\lambda = \frac{\overline{u_i u_i}^{1/2}}{3^{1/2}} \frac{\lambda}{\nu} = \sqrt{\frac{5}{3}} \, \overline{u_i u_i}^*, \tag{2.6}$$

960 A18-4

where λ is given by

$$\lambda = (5\nu)^{1/2} \frac{\overline{u_i u_i}^{1/2}}{\bar{\varepsilon}^{1/2}}. \tag{2.7}$$

The Taylor microscale Reynolds number Re_λ is defined via (2.6), and the Taylor microscale λ is defined via (2.7). Similarly, a more general definition of the local turbulent Péclet number is

$$Pe_{\lambda_\theta} = \frac{\overline{u_i u_i}^{1/2} \lambda_\theta}{\gamma} = (3\,Pr\,\overline{u_i u_i}^* \,\overline{\theta\theta}^*)^{1/2}, \tag{2.8}$$

where

$$\lambda_\theta = (3\gamma)^{1/2} \frac{\overline{\theta\theta}^{1/2}}{\bar{\varepsilon}_\theta^{1/2}} \tag{2.9}$$

is the Corrsin microscale. (Fulachier & Antonia (1983) suggested that the use of u_i, instead of u_1, yields a more meaningful comparison between turbulent Reynolds and Péclet numbers.) After integrating (2.4a,b) twice with respect to x_2^*, we obtain

$$\overline{u_i u_i}^* = x_2^{*2}, \quad \overline{\theta\theta}^* = Pr\,x_2^{*2}. \tag{2.10a,b}$$

Equations (2.10a,b) are tenable as $x_2^* \to 0$ in a channel flow and a boundary layer (figure 14 of Tang & Antonia 2022).

Substituting (2.10a,b) into (2.6) and (2.8), we obtain

$$Re_\lambda = \sqrt{\frac{5}{3}} x_2^{*2}, \quad Pe_{\lambda_\theta} = \sqrt{3}\,Pr\,x_2^{*2}. \tag{2.11a,b}$$

Equations (2.11a,b) indicate that both Re_λ and Pe_{λ_θ} should be independent of Re_τ as $x_2^* \to 0$ (at a given Pr). On the other hand, in the region sufficiently far away from the wall where the effect of the wall on the flow is negligible (e.g. the central region of the channel or pipe), both Re_λ and Pe_{λ_θ} should go to infinity when Re_τ and $Pr\,Re_\tau$ go to infinity; hereafter, this region will be described as $x_2^* \to \delta^*$. It is expected that both Re_λ and Pe_{λ_θ} cannot increase to infinity abruptly at small and moderate x_2^*. Consequently, there should be a near-wall region over which $\overline{u_i u_i}$ and $\overline{\theta\theta}$, after normalization by $\bar{\varepsilon}$, $\bar{\varepsilon}_\theta$ and ν, increase with x_2^* at sufficiently high Re_τ and $Pr\,Re_\tau$; this increase should not depend on Re_τ at a given Pr. Further, at a sufficiently, though not infinitely, large distance from the wall ($0 \ll x_2^* \ll \delta^*$) where the effect of ν is negligible, $\overline{u_i u_i}$ and $\overline{\theta\theta}$ should be determined by $\bar{\varepsilon}$ and $\bar{\varepsilon}_\theta$. Dimensional analysis leads to $\overline{u_i u_i}^* = C_q x_2^{*2/3}$ and $\overline{\theta\theta}^* = C_\theta x_2^{*2/3}$, over which an inertial-convective range is established; the details can be found in Appendix A. Here, C_q and C_θ are constants. Finally, at large Pr, there should be a range between the inertial-convective range (at moderate x_2^*) and the viscous-diffusive range (at small x_2^*) over which the effect of viscosity, instead of diffusivity, is important. The previous arguments are best summarized by the following hypothesis.

In wall turbulence at sufficiently high Reynolds and Péclet numbers, velocity and passive scalar fluctuation statistics, such as $\overline{u_i u_i}$, $\overline{u_i u_j}$ and $\overline{\theta\theta}$, do not depend on the Reynolds and Péclet numbers when the normalization uses $\bar{\varepsilon}$, $\bar{\varepsilon}_\theta$ and ν. Consequently, they are independent of the Reynolds and Péclet numbers. In other words, they depend only on the distance from the wall. Further, at a sufficiently large distance from the wall where the effect of ν is negligible, $\overline{u_i u_i}$, $\overline{u_i u_j}$ and $\overline{\theta\theta}$ are determined by $\bar{\varepsilon}$ and $\bar{\varepsilon}_\theta$. Finally, there is a viscous-convective range for $\overline{\theta\theta}$ between the viscous-diffusion and inertial-convective

ranges over which the effect of ν, instead of γ, is important when the Prandtl number is sufficiently large. The larger the Reynolds and Péclet numbers, the larger the distance from the wall over which the above hypothesis applies.

Whilst it is tempting to hypothesize that in the wall region, $\overline{u_i u_i}^*$, $\overline{u_i u_j}^*$ and $\overline{\theta \theta}^*$ should not depend significantly on the flow type (especially when the outer boundary conditions are similar, such as for the pipe and the channel), we refrain from doing so at this stage. We will, however, test the above hypothesis in all three canonical flows, i.e. the channel, boundary layer and pipe.

Mathematically, the hypothesis predicts that in wall turbulence, the behaviour of $\overline{u_i u_j}$, $\overline{u_i u_i}$ and $\overline{\theta \theta}$ can be expressed as

$$\overline{u_i u_j}^* = f_{ij}(x_2^*), \quad \overline{u_i u_i}^* = f_q(x_2^*), \quad \overline{\theta \theta}^* = f_\theta(x_2^*), \qquad (2.12a\text{–}c)$$

where the asterisk denotes normalization by $\bar{\varepsilon}$, $\bar{\varepsilon}_\theta$ and ν (or equivalently, θ_B, u_K and η), and the functions f_{ij}, f_q and f_θ are independent of the Reynolds and Péclet numbers once appropriate values of the Reynolds and Péclet numbers are reached. A conceptual sketch of the predictions for $|\overline{u_i u_j}^*|$, $\overline{u_i u_i}^*$ and $\overline{\theta \theta}^*$ at $Pr \approx 1$ is shown in figure 2 using log–log scales. Also shown in this figure is a sketch for $\overline{\theta \theta}^*$ at large Pr. At small x_2^*, there should be a viscous-diffusive dominated range for $\overline{u_i u_j}^*$, $\overline{u_i u_i}^*$ and $\overline{\theta \theta}^*$. In the inertial-convective range $0 \ll x_2^* \ll \delta^*$,

$$\overline{u_i u_j}^* = C_{ij} x_2^{*2/3}, \quad \overline{u_i u_i}^* = C_q x_2^{*2/3}, \quad \overline{\theta \theta}^* = C_\theta x_2^{*2/3}, \qquad (2.13a\text{–}c)$$

where C_{ij} is constant; the detailed derivations in the context of $\overline{u_i u_i}^*$ and $\overline{\theta \theta}^*$ can be found in Appendix A. Finally, at large Pr, there exists a viscous-convective range for $\overline{\theta \theta}$ between the inertial-convective range and the viscous-diffusive range. We assume that $\overline{\theta \theta}/\bar{\varepsilon}_\theta$ scales with the Kolmogorov time scale $(\nu/\bar{\varepsilon})^{1/2}$, which leads to

$$\overline{\theta \theta}^* = const. \qquad (2.14)$$

We will test (2.12a–c)–(2.14) in § 3.

3. Test of the hypothesis

Figure 3 shows the Kolmogorov-normalized turbulent kinetic energies $\overline{u_i u_i}^*$ in the channel, boundary layer and pipe for $Re_\tau = 445$–10^4. They are plotted using the wall-parameter-normalized $\overline{u_i u_i}^+$ in these three flows (Simens *et al.* 2009; Jiménez *et al.* 2010; Borrell, Sillero & Jiménez 2013; Sillero, Jiménez & Moser 2013; Lee & Moser 2015, 2019; Pirozzoli *et al.* 2021; Hoyas *et al.* 2022). Specifically, the horizontal axis x_2^* is obtained via $x_2^* = x_2^+/\eta^+ = x_2^+ \bar{\varepsilon}^{+1/4}$, and the vertical axis $\overline{u_i u_i}^*$ is obtained via $\overline{u_i u_i}^* = \overline{u_i u_i}^+/u_K^{+2} = \overline{u_i u_i}^+/\bar{\varepsilon}^{+1/2}$. For clarity, we show in a separate figure (figure 4) the distributions of Kaneda & Yamamoto (2021) in the channel flow over a relatively large range of Re_τ (= 500–8000); the distribution at $Re_\tau = 2000$ for the channel flow in figure 3 is added in figure 4 for reference. It can be seen from figures 3 and 4 that $\overline{u_i u_i}^*$ collapses nearly perfectly for $x_2^* \lesssim 1$ in all wall flows over a wide range of Re_τ (= 445–10^4). The larger the Reynolds number, the wider the x_2^* range over which $\overline{u_i u_i}^*$ is approximately independent of the type of flow as well as of Re_τ; this can be seen more clearly in the linear–log scales (see figures 3(*b*) and 4(*b*)). In particular, the collapse of the $\overline{u_i u_i}^*$ distribution at $Re_\tau = 5200$ with the distribution at $Re_\tau = 10^4$ can extend to $x_2^* \approx 4$. This collapse can also be seen from figure 5, which shows the variation of $\overline{u_i u_i}^*$ at two
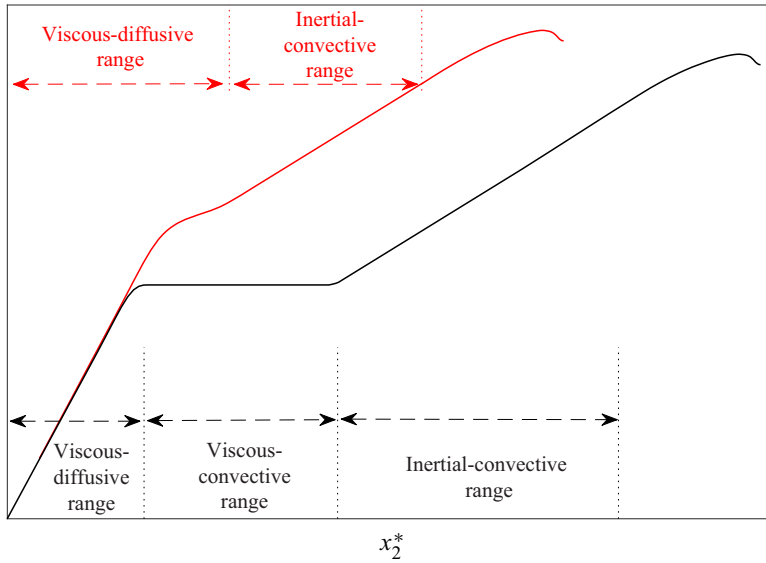
960 A18-6

Figure 2. Predictions for $|\overline{u_i u_j}^*|$, $\overline{u_i u_i}^*$ and $\overline{\theta\theta}^*$ at $Pr \approx 1$ on log–log scales (red curve). Also shown, based on the present hypothesis, is the prediction for $\overline{\theta\theta}^*$ at large Pr (black curve).

typical locations: $x_2^* = 4$ and 9, on Re_τ in all wall flows. There is a clear Re_τ dependence of $\overline{u_i u_i}^*$ at $x_2^* = 9$ when Re_τ is small to moderate (<5200); this dependence becomes very small, if not negligible, when $Re_\tau > 5200$. In contrast, $\overline{u_i u_i}^*$ at $x_2^* = 4$ increases slightly as Re_τ increases, eventually becoming constant for $Re_\tau \gtrsim 2000$. This confirms that the approximate independence of $\overline{u_i u_i}^*$ on the flow and Re_τ in figures 3 and 4 extends to $x_2^* \approx 4$ when $Re_\tau \gtrsim 2000$. It is worth mentioning that the variation of x_2^* with x_2^+ in a channel for $Re_\tau = 550$–10^4 has been presented and discussed by Tang & Antonia (2022) (see their figure 2). At $Re_\tau = 10^4$, $x_2^* = 4$ and 9 correspond to $x_2^+ = 6.3$ and 14.8, respectively. For reference, the corresponding x_2^+ values, with an increment of 0.5 decade, at $Re_\tau = 10^4$ are added onto the upper abscissa of figure 3.

Figure 6 shows the local slope of $\overline{u_i u_i}^*$, i.e. $LS_k(x_2^*) = \mathrm{d} \log \overline{u_i u_i}^*(x_2^*)/\mathrm{d} \log x_2^*$ in the channel flow. For clarity, only the channel data in figure 3 are shown in this figure. The collapse of $LS_k(x_2^*)$ at small x_2^* is not surprising because of the collapse of $\overline{u_i u_i}^*$ at small x_2^*. In particular, $LS_k(x_2^*) \to 2$ as $x_2^* \to 0$; see figure 6 or (2.10a,b). At the moderate x_2^*, say $x_2^* \sim 30$, although $\overline{u_i u_i}^*$ does not collapse (figures 3 and 4), its slope increases with Re_τ, gradually approaching the 2/3 power-law scaling. We can see this behaviour more clearly in figure 6, where the local slope $LS_k(x_2^*)$ increases systematically with Re_τ, and the 2/3 power-law scaling is approached by the distribution at $Re_\tau = 10^4$ over the range $30 \lesssim x_2^* \lesssim 70$. In this x_2^* range at $Re_\tau = 10^4$, $\overline{u_i u_i}^* \approx C_q x_2^{*2/3} = 5.807 x_2^{*2/3}$, although it is not clear whether the prefactor (C_q) has become Re_τ-independent; higher Re_τ data are needed. In contrast, the variation of the wall-parameter-normalized $\overline{u_i u_i}^+$ with Re_τ is systematic at all x_2^+ in the channel, boundary layer and pipe (figure 7).
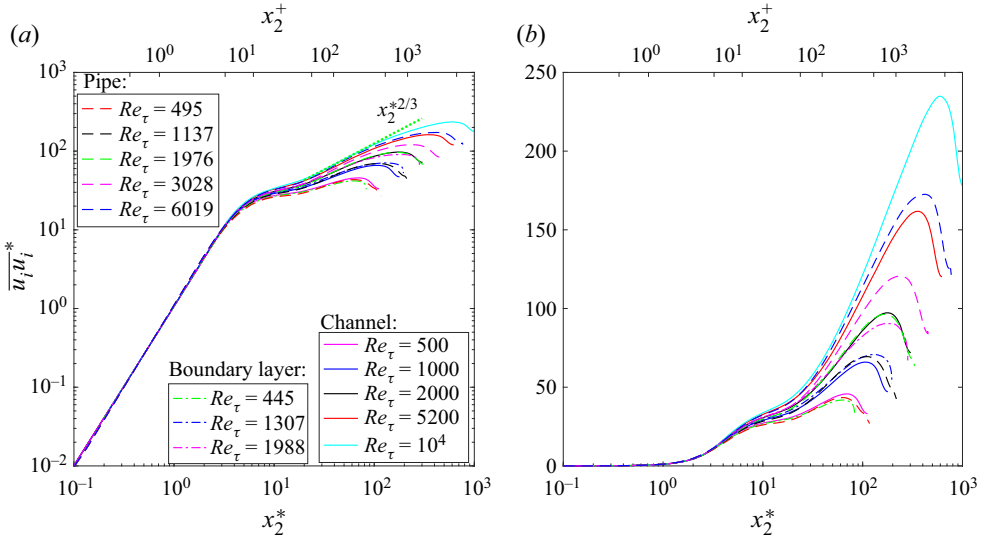
960 A18-7

Figure 3. (a) Kolmogorov-normalized turbulent kinetic energies $\overline{u_i u_i}^*$ in a channel (Lee & Moser 2015, 2019; Hoyas *et al.* 2022), boundary layer (Simens *et al.* 2009; Jiménez *et al.* 2010; Borrell *et al.* 2013; Sillero *et al.* 2013) and pipe (Pirozzoli *et al.* 2021). They are plotted using wall-parameter normalization in those three flows, using the relations $x_2^* = x_2^+/\eta^+ = x_2^+ \bar{\varepsilon}^{+1/4}$ and $\overline{u_i u_i}^* = \overline{u_i u_i}^+/u_K^{+2} = \overline{u_i u_i}^+/\bar{\varepsilon}^{+1/2}$. The green dotted line indicates $\sim x_2^{*2/3}$. Note that the data close to and beyond the edge of the boundary layer ($x_2/\delta > 0.8$) are not shown since they are affected by the intermittency associated with the turbulent/potential flow interface. (b) Corresponding distributions on linear–log scales. For reference, the corresponding x_2^+ values, with increment 0.5 decade, at $Re_\tau = 10^4$ are added on the upper abscissa. Note that the variation of x_2^+ with x_2^* is nonlinear; see figure 2 of Tang & Antonia (2022).
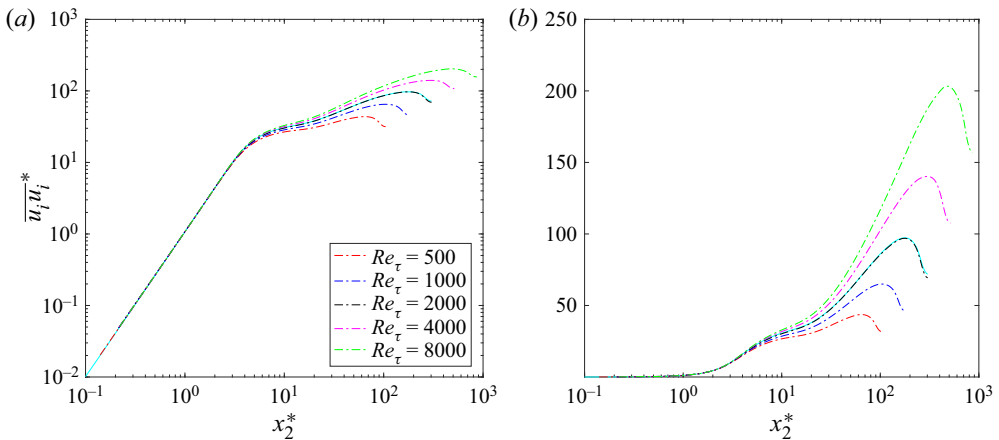

Figure 4. (a) Kolmogorov-normalized $\overline{u_i u_i}^*$ in a channel. They are plotted using the wall-parameter-normalized $\overline{u_i u_i}^+$ of Kaneda & Yamamoto (2021). For reference, also shown in this figure (cyan curve) is the distribution of Lee & Moser (2015, 2019) at $Re_\tau = 2000$ in figure 3. (b) Corresponding distributions on linear–log scales.

We next focus on the behaviour of the Reynolds stresses $\overline{u_i u_j}^*$. Note that in the region $x_2 \to 0$ (e.g. Pope 2000),

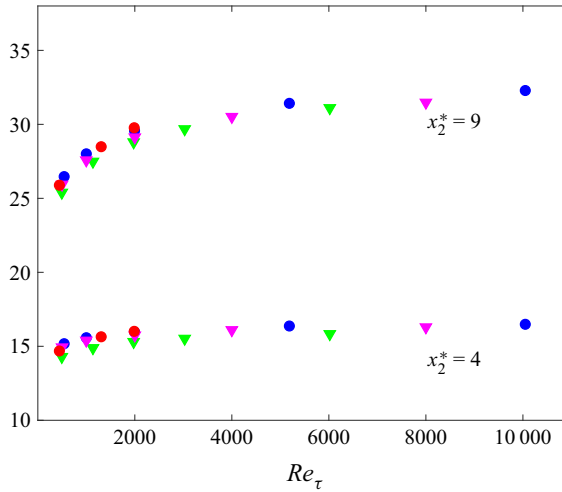$$\bar{\varepsilon}_{ij} = \nu \frac{\partial^2 \overline{u_i u_j}}{\partial x_2^2}, \tag{3.1}$$

Figure 5. Dependence of $\overline{u_i u_i}^*$ on Re_τ at $x_2^* = 9$ and 4, corresponding to the data in figures 3 and 4. Pipe: ▽, green (Pirozzoli *et al.* 2021). Channel: ○, blue (Lee & Moser 2015, 2019; Hoyas *et al.* 2022); ▽, magenta (Kaneda & Yamamoto 2021). Boundary layer: ○, red (Simens *et al.* 2009; Jiménez *et al.* 2010; Borrell *et al.* 2013; Sillero *et al.* 2013).
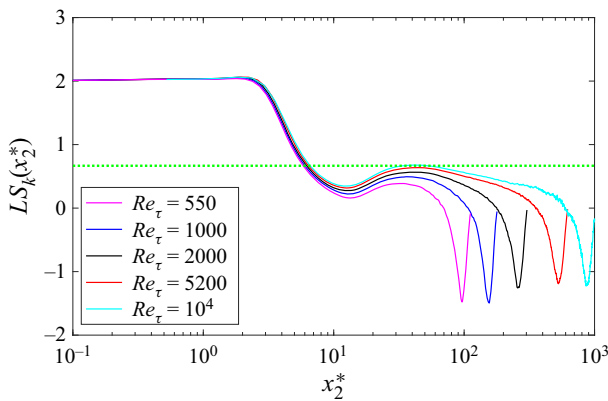

Figure 6. Local slope of $\overline{u_i u_i}^*$, i.e. $LS_k(x_2^*) = \mathrm{d} \log \overline{u_i u_i}^*(x_2^*)/\mathrm{d} \log x_2^*$, corresponding to the channel data in figure 3. The green dotted line corresponds to the value 2/3.

where $\bar{\varepsilon}_{ij}$ is the dissipation rate tensor, which is given by

$$\bar{\varepsilon}_{ij} = 2\nu \overline{\left(\frac{\partial u_i}{\partial x_k} \frac{\partial u_j}{\partial x_k} \right)}. \tag{3.2}$$

After normalizing by the Kolmogorov scales, (3.1) can be rewritten as

$$\bar{\varepsilon}_{ij}^* = \frac{\partial^2 \overline{u_i u_j}^*}{\partial x_2^{*2}}. \tag{3.3}$$

Since $u_2 \sim x_2^2$ as $x_2 \to 0$ (e.g. Pope 2000), $\bar{\varepsilon}_{22}^*$ and $\bar{\varepsilon}_{12}^*$, and the corresponding quantities on the right-hand side of (3.3), should be zero as $x_2 \to 0$. On the other hand, Tang & Antonia (2022) showed that $\bar{\varepsilon}_{11}^*$ and $\bar{\varepsilon}_{33}^*$ become Re_τ-independent when $Re_\tau > 1000$ in
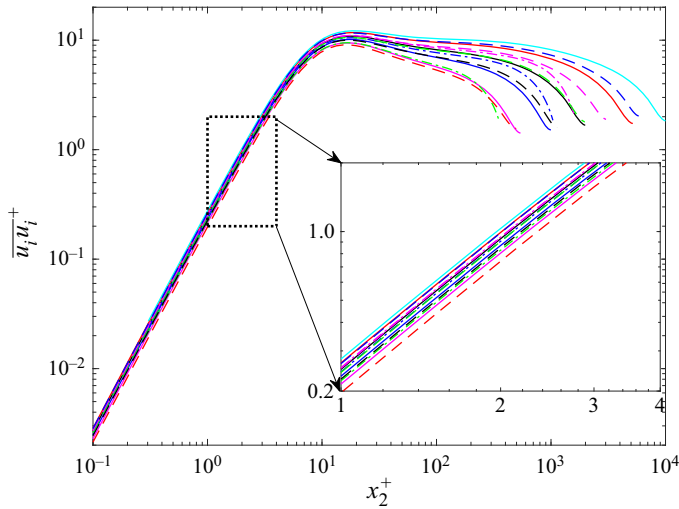
960 A18-9

Figure 7. Wall-parameter-normalized $\overline{u_i u_i}^+$ in a channel, boundary layer and pipe for the same data as in figure 3. The inset zooms in on the range $x_2^+ = 1\text{–}4$.

the channel and boundary layer. One thus expects that, based on (3.3), $\overline{u_i u_j}^*$ should be Re_τ-independent as $x_2^* \to 0$, at least for $i = j = 1$ and $i = j = 3$. Since $Re_\tau > 1000$ is required for $\bar{\varepsilon}_{11}^*$ and $\bar{\varepsilon}_{33}^*$ to become Re_τ-independent in the channel and boundary layer (Tang & Antonia 2022), we show in figure 8 the Kolmogorov-normalized distributions $\overline{u_1 u_1}^*$, $\overline{u_2 u_2}^*$, $\overline{u_3 u_3}^*$ and $\overline{u_1 u_2}^*$ in these two flows for only $Re_\tau > 1000$ for the data of Simens *et al.* (2009), Jiménez *et al.* (2010), Borrell *et al.* (2013), Sillero *et al.* (2013), Lee & Moser (2015, 2019) and Hoyas *et al.* (2022). For clarity, we show in a separate figure (figure 9) the channel data of Kaneda & Yamamoto (2021) at $Re_\tau = 2000$, 4000 and 8000; the distribution for the same flow at $Re_\tau = 2000$ in figure 8 has been added to figure 9 for reference. Although the distributions for $\bar{\varepsilon}_{11}^*$ and $\bar{\varepsilon}_{33}^*$ in the pipe for $Re_\tau \gtrsim 2000$ are not available, we show in figure 9 the distributions of $\overline{u_i u_j}^*$ in the pipe for a similar Reynolds number range as in the channel, namely $Re_\tau \gtrsim 2000$. There is a nearly perfect collapse for all distributions in figure 8 at small x_2^*. Specifically, the collapse of $\overline{u_1 u_1}^*$, $\overline{u_2 u_2}^*$, $\overline{u_3 u_3}^*$ and $\overline{u_1 u_2}^*$ extends to $x_2^* \approx 4$, 40, 4 and 40, respectively. The same observations can also be made from figure 9 for the channel and pipe. Namely, the x_2^* range over which $\overline{u_i u_j}^*$ distributions collapse is approximately one order of magnitude larger for $\overline{u_2 u_2}^*$ and $\overline{u_1 u_2}^*$ than for $\overline{u_1 u_1}^*$ and $\overline{u_3 u_3}^*$. This can also be observed in figure 10, which shows the magnitudes of $\overline{u_1 u_1}^*$ and $\overline{u_3 u_3}^*$ at $x_2^* = 4$ and 9 versus Re_τ, and those of $\overline{u_2 u_2}^*$ and $\overline{u_1 u_2}^*$ at $x_2^* = 40$ and 90 versus Re_τ in the three wall flows. Evidently, there is a clear Re_τ dependence for $\overline{u_1 u_1}^*$ and $\overline{u_3 u_3}^*$ at $x_2^* = 9$, and for $\overline{u_2 u_2}^*$ and $\overline{u_1 u_2}^*$ at $x_2^* = 90$, when Re_τ is small to moderate (<5200); this dependence becomes very small when $Re_\tau > 5200$. However, the distributions at $x_2^* = 4$ for $\overline{u_1 u_1}^*$ and $\overline{u_3 u_3}^*$, and those at $x_2^* = 40$ for $\overline{u_2 u_2}^*$ and $\overline{u_1 u_2}^*$, are approximately constant for $Re_\tau \gtrsim 2000$. The above observations indicate that the x_2^* range over which $\overline{u_i u_j}^*$ collapses depends on the specific quantity. It is worth mentioning that a close look at the distributions of $\overline{u_2 u_2}^*$ and $\overline{u_1 u_2}^*$ in figure 9 shows that there is a very small difference between the channel and the pipe in the range $x_2^* \lesssim 5$. Note that the magnitudes of $\overline{u_2 u_2}^*$ and $\overline{u_1 u_2}^*$ are approximately 1–2 orders of magnitude smaller than those of $\overline{u_1 u_1}^*$ and $\overline{u_3 u_3}^*$. This small difference is likely due to the different resolutions of the simulations between these two flows.
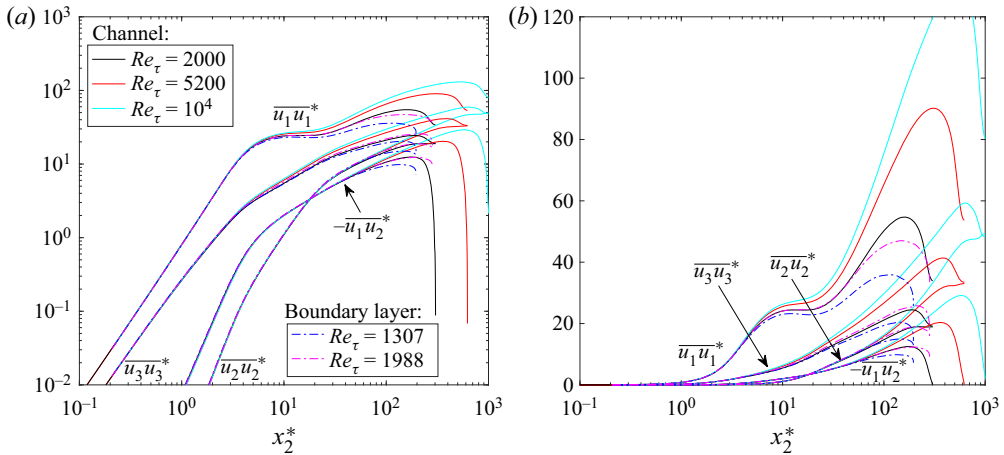
960 A18-10

Figure 8. (*a*) Kolmogorov-normalized $\overline{u_1u_1}^*$, $\overline{u_2u_2}^*$, $\overline{u_3u_3}^*$ and $\overline{u_1u_2}^*$ in the channel and boundary layer for $Re_\tau > 1000$. They are plotted using the wall-parameter-normalized $\overline{u_iu_j}^+$ in these two flows (Simens *et al.* 2009; Jiménez *et al.* 2010; Borrell *et al.* 2013; Sillero *et al.* 2013; Lee & Moser 2015, 2019; Hoyas *et al.* 2022). (*b*) Corresponding distributions on linear–log scales.
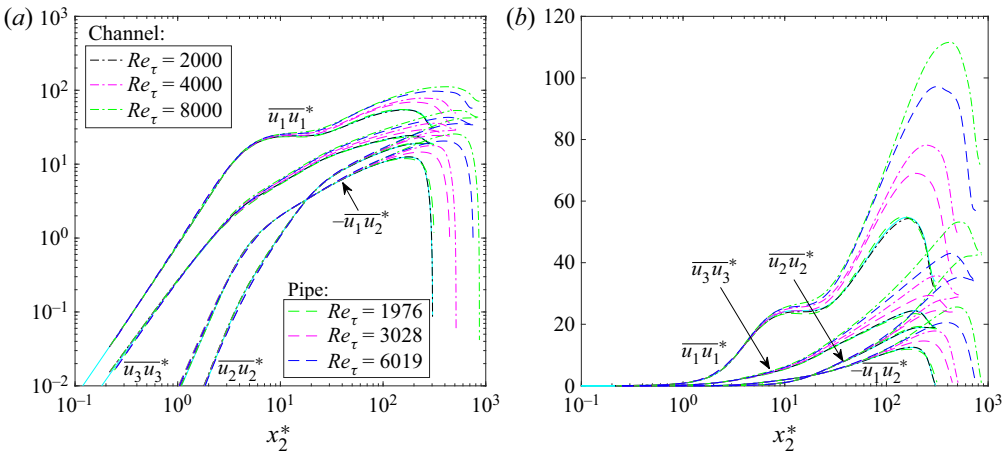

Figure 9. (*a*) Kolmogorov-normalized $\overline{u_1u_1}^*$, $\overline{u_2u_2}^*$, $\overline{u_3u_3}^*$ and $\overline{u_1u_2}^*$ in the channel and pipe for $Re_\tau \gtrsim 2000$. They are plotted using the wall-parameter-normalized $\overline{u_iu_j}^+$ in these two flows (Kaneda & Yamamoto 2021; Pirozzoli *et al.* 2021). For reference, also shown (cyan curves) are the distributions of Lee & Moser (2015, 2019) at $Re_\tau = 2000$ in figure 8. (*b*) Corresponding distributions on linear–log scales.

Another important feature of the distributions in figures 8–10 is the increased extent of the collapse with increasing Re_τ. This can also be observed in figure 11, which shows the corresponding local slope of $\overline{u_iu_j}^*$, i.e. $LS_{u_iu_j}(x_2^*) = \mathrm{d}\log\overline{u_iu_j}^*(x_2^*)/\mathrm{d}\log x_2^*$ in the channel flow at $Re_\tau = 5200$ and 10^4, respectively. The local slope for $\overline{u_1u_1}^*$ at $Re_\tau = 10^4$ approaches 2/3 over the range $35 \lesssim x_2^* \lesssim 70$. This behaviour is similar to that for $\overline{u_iu_i}^*$ (see figure 6) since $\overline{u_1u_1}^*$ is the largest contribution to $\overline{u_iu_i}^*$ (figure 8). In contrast, $\overline{u_2u_2}^*$ and $\overline{u_3u_3}^*$ make relatively small contributions to $\overline{u_iu_i}^*$ at small to moderate x_2^*, thus their behaviours are unlikely to affect $\overline{u_iu_i}^*$ significantly. Accordingly, the distributions of $LS_{u_3u_3}$ do not approach 2/3, while those of $LS_{u_2u_2}$ do not deviate significantly from 2/3 over

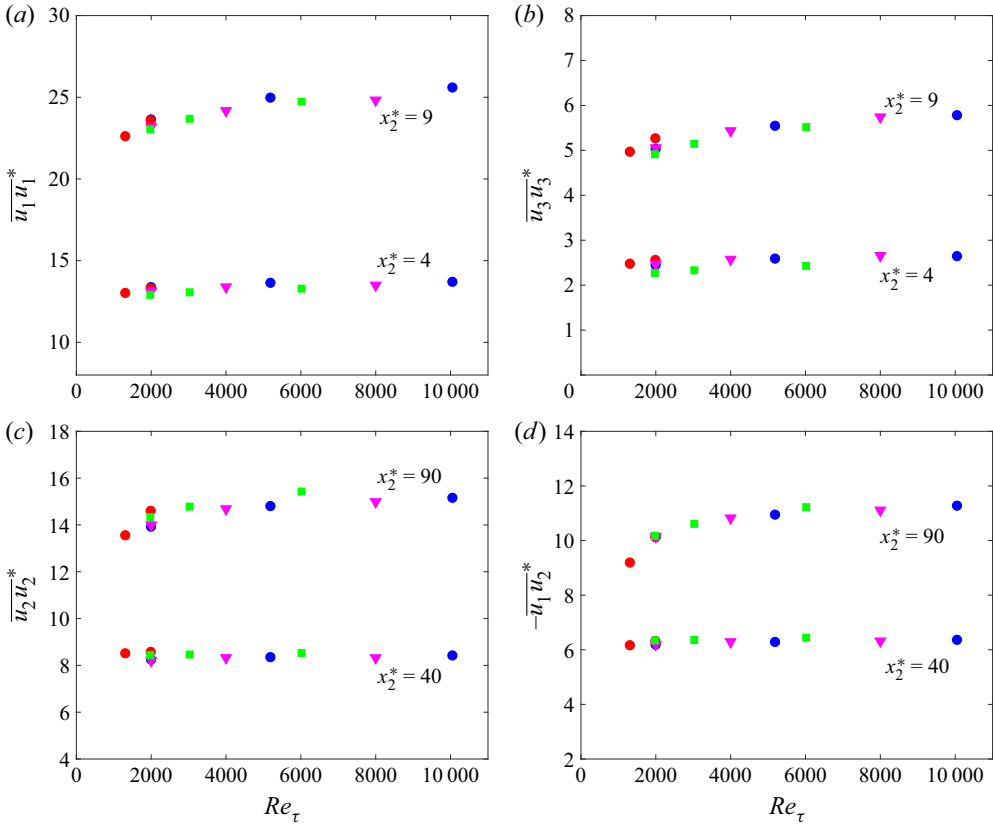Figure 10. (*a,b*) Dependence of $\overline{u_1 u_1}^*$ and $\overline{u_3 u_3}^*$ on Re_τ at $x_2^* = 9$ and 4. (*c,d*) Dependence of $\overline{u_2 u_2}^*$ and $-\overline{u_1 u_2}^*$ on Re_τ at $x_2^* = 90$ and 40. Pipe: □, green (Pirozzoli *et al.* 2021). Channel: ∘, blue (Lee & Moser 2015, 2019; Hoyas *et al.* 2022); ▽, magenta (Kaneda & Yamamoto 2021). Boundary layer: ∘, red (Simens *et al.* 2009; Jiménez *et al.* 2010; Borrell *et al.* 2013; Sillero *et al.* 2013).

the range $70 \lesssim x_2^* \lesssim 170$ at $Re_\tau = 10^4$. Note that the local slopes of $\overline{u_1 u_1}^*$, $\overline{u_2 u_2}^*$, $\overline{u_3 u_3}^*$ and $\overline{u_1 u_2}^*$ approach 2, 4, 2 and 3, respectively, as $x_2^* \to 0$. This is not surprising since $u_1 \sim u_3 \sim x_2$ and $u_2 \sim x_2^2$ as $x_2 \to 0$ (e.g. Pope 2000). Overall, figures 3–11 provide good support for the present hypothesis in the context of the Reynolds stresses and the turbulent kinetic energy. Evidently, it would be desirable to investigate further the finite Reynolds number effect on $\overline{u_i u_i}^*$ and $\overline{u_i u_j}^*$ at moderate x_2^* by further increasing Re_τ.

We conclude this section by examining the dependence on Re_τ and Pr of $\overline{\theta\theta}^*$. Figure 12 shows the distributions of $\overline{\theta\theta}^*/Pr$ in the channel at $Re_\tau = 500, 1000, 2000$ and 5000, and $Pr = 0.01, 0.1, 0.71, 2$ and 7, respectively. For clarity, the corresponding local slopes of $\overline{\theta\theta}^*$, i.e. $LS_\theta(x_2^*) = \mathrm{d}\log\overline{\theta\theta}^*(x_2^*)/\mathrm{d}\log x_2^*$, for only $Pr = 0.71$ and 7, and for $Re_\tau \geq 1000$, are shown in figure 13. We can observe from figure 12 that the relation $\overline{\theta\theta}^*/Pr = x_2^{*2}$ (see (2.10*b*)) is satisfied adequately at all Re_τ and Pr (note that the Péclet number is equal to $Re_\tau Pr$) over a significant range of x_2^*. An overall feature of this figure is that at a given Pr, the collapse extends to increasingly larger values of x_2^* as Re_τ increases. In particular, at $Pr = 7$, the collapse appears to extend to $x_2^* \approx 10$. More importantly, there is an approximate plateau, of value approximately 37.5, over the range $3 \lesssim x_2^* \lesssim 9$, indicating an emergence of a viscous-convective range, which is weakly affected by γ. This can also
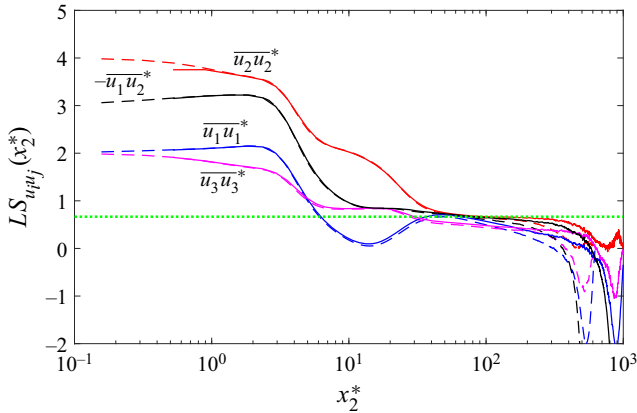
960 A18-12

Figure 11. Local slope of $\overline{u_i u_j}^*$, i.e. $LS_{u_i u_j}(x_2^*) = \mathrm{d} \log \overline{u_i u_j}^*(x_2^*)/\mathrm{d} \log x_2^*$; for clarity, only the channel data at $Re_\tau = 5200$ (dashed curves) and 10^4 (solid curves) are shown. The green dotted line corresponds to the value $2/3$.
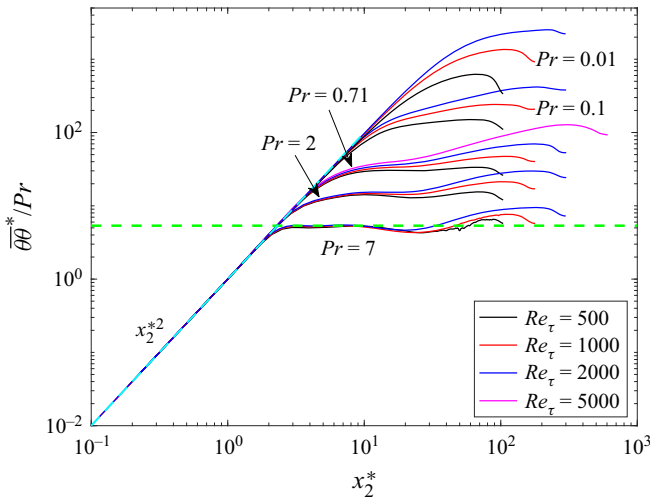

Figure 12. Batchelor–Kolmogorov normalized $\overline{\theta\theta}^*/Pr$ in a channel. They are plotted using the wall-parameter-normalized $\overline{\theta\theta}^+$ (Alcántara-Ávila *et al.* 2018, 2021; Lluesma-Rodríguez *et al.* 2018; Alcántara-Ávila & Hoyas 2021). Cyan curve shows x_2^{*2}. The green dashed line corresponds to the value 37.5. Note that the $\bar{\varepsilon}^+$ distributions of Lee & Moser (2015, 2019) at nearly the same Re_τ (550, 1000, 2000 and 5200) are used for normalization since the values of $\bar{\varepsilon}^+$ for Alcántara-Ávila *et al.* (2018, 2021), Lluesma-Rodríguez *et al.* (2018) and Alcántara-Ávila & Hoyas (2021) are not available.

be seen in figure 13, which shows that the corresponding local slope of $\overline{\theta\theta}^*$ is close to 0 in the same x_2^* range at $Pr = 7$ and $Re_\tau \geq 1000$. Over the range $30 \lesssim x_2^* \lesssim 100$, there is a clear Re_τ dependence for almost all distributions of $\overline{\theta\theta}^*/Pr$ at any Pr (see figure 12). The magnitude of LS_θ at $Pr = 0.71$ also increases systematically with Re_τ in this range (figure 13). Even at the highest Re_τ (=5000), the $2/3$ power-law scaling predicted by the present hypothesis is not approached. Similarly, at a larger Pr (=7) but a smaller Re_τ (=2000), the distribution of LS_θ does not yet exhibit a plateau corresponding to $2/3$. Evidently, larger values of Re_τ and Pr are required to establish the $2/3$ power-law
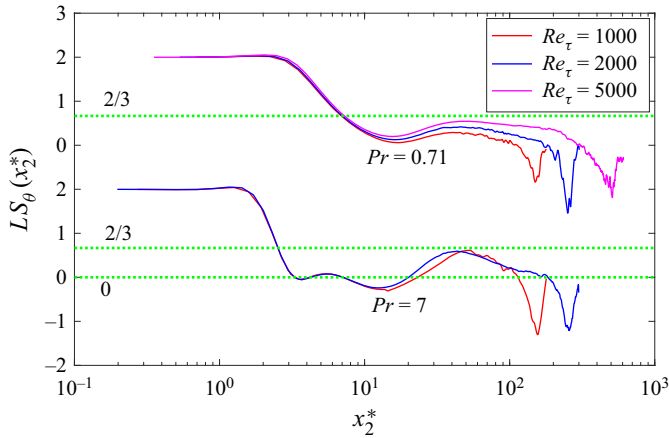
960 A18-13

Figure 13. Local slope of $\overline{\theta\theta}^*$, i.e. $LS_\theta(x_2^*) = \mathrm{d}\log\overline{\theta\theta}^*(x_2^*)/\mathrm{d}\log x_2^*$, corresponding to the data in figure 12; for clarity, only the data at $Pr = 0.71$, 7 and for $Re_\tau \geq 1000$ are shown. The green dotted lines correspond to the values 2/3 and 0.

scaling for $\overline{\theta\theta}^*$ unequivocally. It is worth mentioning that in figure 12, we have used the $\bar{\varepsilon}^+$ distributions of Lee & Moser (2015, 2019) at nearly the same Re_τ (550, 1000, 2000 and 5200) for normalization since the values of $\bar{\varepsilon}^+$ for Alcántara-Ávila, Hoyas & Pérez-Quiles (2018), Lluesma-Rodríguez, Hoyas & Perez-Quiles (2018), Alcántara-Ávila *et al.* (2021) and Alcántara-Ávila & Hoyas (2021) are not available. We should stress that the use of a different $\bar{\varepsilon}^+$ distribution will not affect the results in figure 12; this has been discussed previously (Tang & Antonia (2022), see their appendix A) in the context of the transport equation for $\bar{\varepsilon}_\theta$. Following Tang & Antonia (2022), when we normalize the data in figure 12 by using the $\bar{\varepsilon}^+$ data of Bernardini, Pirozzoli & Orlandi (2014) at $Re_\tau = 550$, 1000 and 2000, the resulting distributions (not shown here) cannot be distinguished from those in figure 12.

4. Relationship to the wall scaling

We recall that the scaling of the mean velocity and mean scalar based on wall parameters near the wall has received strong support in the literature. This is, however, not the case for $\overline{u_i u_j}^+$, $\overline{u_i u_i}^+$ and $\overline{\theta\theta}^+$, at least at finite Re_λ. The evidence presented above indicates that near the wall, the scaling of $\overline{u_i u_j}$, $\overline{u_i u_i}$ and $\overline{\theta\theta}$ based on $\bar{\varepsilon}$, $\bar{\varepsilon}_\theta$ and ν is superior to that based on wall parameters. The relationship between the wall parameters and $\bar{\varepsilon}$, $\bar{\varepsilon}_\theta$ and ν can be quantified by the wall-parameter-normalized $\bar{\varepsilon}$ and $\bar{\varepsilon}_\theta$, i.e. $\bar{\varepsilon}^+$ and $\bar{\varepsilon}_\theta^+$. Figure 14(*a*) shows the distributions of $\bar{\varepsilon}^+$ and $x_2^+\bar{\varepsilon}^+$ in a pipe for $Re_\tau = 495$–6019; the latter allows the collapse of $\bar{\varepsilon}^+$ distributions (if it exists) at large x_2^+ to be examined more closely. An overall feature of figure 14(*a*) is that the magnitudes of $\bar{\varepsilon}^+$ and $x_2^+\bar{\varepsilon}^+$ become increasingly close to each other over a large range of x_2^+ with increasing Re_τ. The same feature can also be observed in the channel for $Re_\tau = 550$–10^4 (see figure 1 of Tang & Antonia 2022). In contrast, there is a nearly perfect collapse for the distributions of $\bar{\varepsilon}^+$ and $x_2^+\bar{\varepsilon}^+$ over the range $10 \lesssim x_2^+ \lesssim 30$ for $Re_\tau = 445$–1988 in the boundary layer (figure 14*b*). We report in figure 15 the distributions of $\bar{\varepsilon}_\theta^+$ and $x_2^+\bar{\varepsilon}_\theta^+$ in the channel for $Re_\tau = 500$–5000. We can observe that the $\bar{\varepsilon}_\theta^+$ and $x_2^+\bar{\varepsilon}_\theta^+$ distributions collapse over the
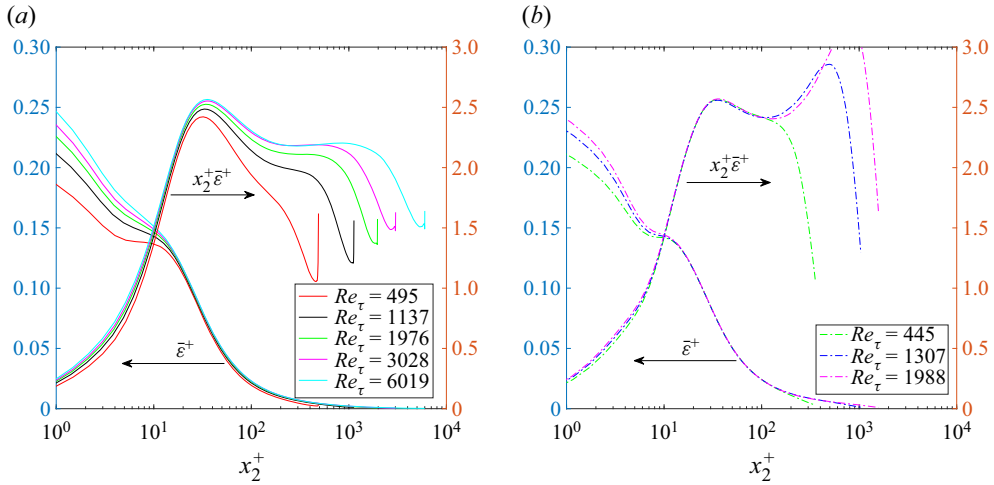
960 A18-14

Figure 14. Distributions of $\bar{\varepsilon}^+$ and $x_2^+\bar{\varepsilon}^+$ in (*a*) the pipe, and (*b*) the boundary layer. They are plotted using the data of Simens *et al.* (2009), Jiménez *et al.* (2010), Borrell *et al.* (2013), Sillero *et al.* (2013) and Pirozzoli *et al.* (2021).
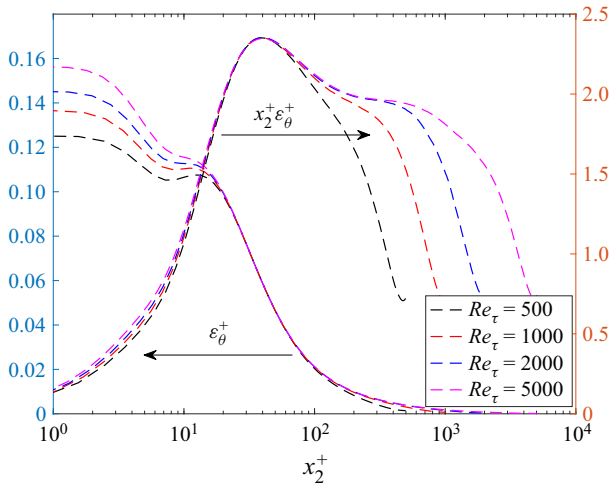

Figure 15. Distributions of $\bar{\varepsilon}_\theta^+$ and $x_2^+\bar{\varepsilon}_\theta^+$ in a channel. They are plotted using the data of Alcántara-Ávila *et al.* (2021).

range $20 \lesssim x_2^+ \lesssim 60$ for $Re_\tau \geq 500$. The collapse appears to extend to larger and smaller values of x_2^+ at higher Re_τ. It is expected that the collapse of $\bar{\varepsilon}^+$ and $x_2^+\bar{\varepsilon}^+$ in the boundary layer should also extend to larger and smaller values of x_2^+ as Re_τ continues to increase (figure 14*b*). On the other hand, the Re_τ independence of $\overline{u_i u_i}^*$, $\overline{u_1 u_1}^*$, $\overline{u_2 u_2}^*$, $\overline{u_3 u_3}^*$, $\overline{u_1 u_2}^*$ and $\overline{\theta\theta}^*$ first emerges at the smallest x_2^* and subsequently at increasingly larger x_2^* as Re_τ increases. Consequently, as Re_τ continues to increase, there should be an x_2 range over which $\overline{u_i u_j}^*$ and $\overline{\theta\theta}^*$ versus x_2^*, and $x_2^+\bar{\varepsilon}^+$ and $x_2^+\bar{\varepsilon}_\theta^+$ versus x_2^+, collapse. Over this range and irrespective of the flow, one should then be able to use the two types of normalization interchangeably.
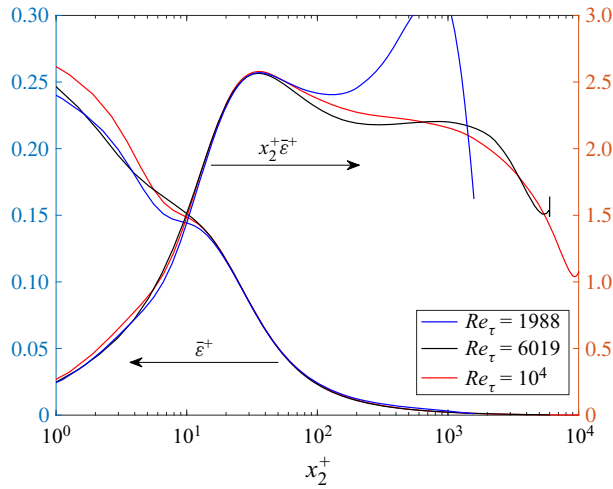
Figure 16. Distributions of $\bar{\varepsilon}^+$ and $x_2^+\bar{\varepsilon}^+$ in a channel ($Re_\tau = 10^4$; Hoyas *et al.* 2022), pipe ($Re_\tau = 6019$; Pirozzoli *et al.* 2021) and boundary layer ($Re_\tau = 1988$; Sillero *et al.* 2013).

Further, although the distributions of $x_2^+\bar{\varepsilon}^+$ in the boundary layer have become Re_τ-independent in the range $10 \lesssim x_2^+ \lesssim 30$ for $Re_\tau \gtrsim 445$ (figure 14b), it is unclear if those of $x_2^+\bar{\varepsilon}^+$ in the pipe flow at $Re_\tau = 6019$ and in the channel flow at $Re_\tau = 10^4$ have become Re_τ-independent in the same x_2^+ range. Nonetheless, it is of interest to compare the $\bar{\varepsilon}^+$ and $x_2^+\bar{\varepsilon}^+$ distributions at the highest Re_τ in the three flows (figure 16). It is remarkable that there is an approximate collapse in the range $12 \lesssim x_2^+ \lesssim 40$. In particular, if the collapse of $\bar{\varepsilon}^+$ and $\bar{\varepsilon}_\theta^+$ can extend to the wall, i.e. at all locations in the range $x_2 \lesssim x_{2\alpha}$, at least in a given wall flow, then $\bar{\varepsilon}^+$ and $\bar{\varepsilon}_\theta^+$ may become bounded at the wall (when $Re_\tau \to \infty$); here, $x_{2\alpha}$ is the upper limit of the range for which there is collapse with respect to $\bar{\varepsilon}^+$ and $\bar{\varepsilon}_\theta^+$. In this situation, the Batchelor–Kolmogorov normalized mean velocity and mean scalar should be Re_τ-independent in the x_2 range $x_2 < \min(x_{2\alpha}, x_{2\alpha_1})$; here, $x_{2\alpha_1}$ is the upper limit of the range in which the wall-parameter-normalized mean velocity and mean scalar collapse. Also, $\overline{u_iu_i}^+$ and $\overline{\theta\theta}^+$ versus x_2^+ should be Re_τ-independent in the x_2 range $x_2 < \min(x_{2\alpha}, x_{2\alpha_2})$; here, $x_{2\alpha_2}$ is the upper limit of the range for which $\overline{u_iu_i}^*$ and $\overline{\theta\theta}^*$ versus x_2^* are Re_τ-independent. This is fully consistent with Chen & Sreenivasan (2021), who suggest that the peak value of $\overline{u_1u_1}^+$ approaches a finite limit as the Reynolds number becomes infinitely large because the dissipation rate at the wall is expected to be bounded.

Since $\bar{\varepsilon}^+$ in a channel, boundary layer and pipe (figures 14 and 1 of Tang & Antonia 2022) and $\bar{\varepsilon}_\theta^+$ in a channel (figure 15) do not collapse as $x_2^+ \to 0$ in the present Re_τ range ($\leq 10^4$), it is expected that the Batchelor–Kolmogorov normalized mean velocity ($\bar{U}_1^*$) and mean scalar (Θ^*) should depend on Re_τ as $x_2^+ \to 0$. As an example, we show in figures 17(a,b) the distributions of $\bar{U}_1^+$ and Θ^+ in a channel at $Pr = 0.71$. It is not surprising that the x_2^+ range over which both $\bar{U}_1^+$ and Θ^+ collapse extends to increasingly larger values of x_2^+ as Re_τ increases. On the other hand, the distributions of θ_B^+ collapse at all Re_τ over the range $20 \lesssim x_2^+ \lesssim 60$, while the u_K^+ distributions appear to collapse approximately at larger Re_τ ($\gtrsim 5200$) over the range $20 \lesssim x_2^+ \lesssim 200$. More importantly,
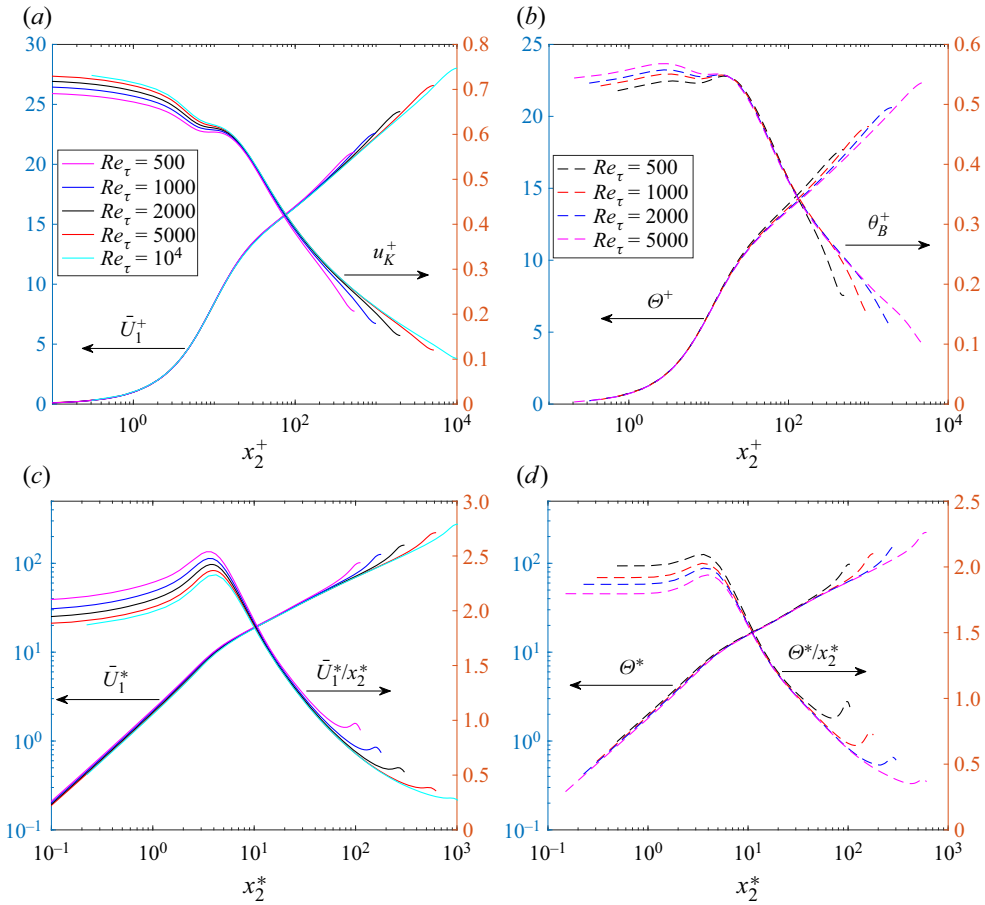
960 A18-16

Figure 17. (*a,b*) Distributions of $\bar{U}_1^+$ and Θ^+ in a channel at $Pr = 0.71$. Also shown are the corresponding distributions of u_K^+ and θ_B^+. (*c,d*) Distributions of $\bar{U}_1^* = \bar{U}_1^+/u_K^+$, $\bar{U}_1^*/x_2^*$, $\Theta^* = \Theta^+/\theta_B^+$ and Θ^*/x_2^*. Data of Lee & Moser (2015, 2019), Alcántara-Ávila *et al.* (2021) and Hoyas *et al.* (2022).

the distributions in figure 17(*a,b*) implies that there should be an x_2^+ ($\gtrsim 20$, or equivalently, $x_2^* \gtrsim 11$) range over which $\bar{U}_1^*$ and Θ^* distributions should be Re_τ-independent. In order to confirm this, we report in figures 17(*c,d*) the distributions of $\bar{U}_1^* = \bar{U}_1^+/u_K^+$ and $\Theta^* = \Theta^+/\theta_B^+$, respectively. Also shown are the same distributions premultiplied by x_2^*, i.e. $\bar{U}_1^*/x_2^*$ and Θ^*/x_2^*, which allow the collapse of $\bar{U}_1^*$ and Θ^* at large x_2^* to be examined more closely. As expected, $\bar{U}_1^*$ for $Re_\tau \gtrsim 5200$, and Θ^* at all Re_τ appears to collapse for $x_2^* \gtrsim 11$; the larger Re_τ is, the wider is the x_2^* range over which $\bar{U}_1^*$ and Θ^* are Re_τ-independent. Only when $\bar{\varepsilon}^+$ and $\bar{\varepsilon}_\theta^+$ (or equivalently, u_K^+ and θ_B^+) become Re_τ-independent at the wall (when $Re_\tau \to \infty$) can one expect $\bar{U}_1^*$ and Θ^* to collapse at the wall. It is worth mentioning that if u_K^+ and θ_B^+ become Re_τ-independent over an x_2^+ range, then $\overline{u_i u_j}^*$ and $\overline{\theta\theta}^*$ should be proportional to $\overline{u_i u_j}^+$ and $\overline{\theta\theta}^+$ at a given x_2^+.

It is well-known that as $Re_\tau \to \infty$, there should be an x_2^+ range (far away from the wall) over which $-\overline{u_1 u_2}^+ = 1$, which should be located in the log-law region. If $\bar{\varepsilon}^+$ collapses in the same x_2^+ range and there is an overlap region over which both $-\overline{u_1 u_2}^+ = 1$ and

960 A18-17

$\overline{u_1 u_2}^* = C_{12} x_2^{*2/3}$ (inertial-convective range) are established unequivocally (again, this may require $Re_\tau \to \infty$), then we can write

$$\overline{u_1 u_2}^* = C_{12}\, x_2^{*2/3} = \frac{\overline{u_1 u_2}^+}{u_K^{+2}} = C_{12}(x_2^+ u_K^+)^{2/3} \quad \Rightarrow \quad u_K^+ = \frac{-1}{C_{12}^{3/8}\, x_2^{+1/4}}. \tag{4.1}$$

Note that the relation $\bar{\varepsilon}^+ = u_K^{+4} = 1/\eta^{+4}$ has been used to derive (4.1), which is consistent with the relation $u_K^+ = (\kappa x_2^+)^{-1/4}$ of Perry, Henbest & Chong (1986) obtained from balancing production and turbulent energy dissipation in the log-law region. It is worth mentioning that one can obtain $\bar{\varepsilon}_\theta^+ \sim 1/x_2^+$ by assuming that the production and dissipation rate of the scalar variance are in balance in the log-law region. If in the overlap region mentioned above (which should be a subrange of both the log-law region and the inertial-convective range) there is 2/3 power-law scaling for $\overline{u_1 u_1}^*$, $\overline{u_2 u_2}^*$, $\overline{u_3 u_3}^*$ and $\overline{\theta\theta}^*$, then it is not difficult to conclude that $\overline{u_1 u_1}^+$, $\overline{u_2 u_2}^+$, $\overline{u_3 u_3}^+$, $\overline{u_i u_i}^+$ and $\overline{\theta\theta}^+$ should be constant. As examples, $\overline{u_i u_i}^+$ and $\overline{\theta\theta}^+$, after normalizing the first equations in (A5) and (A6), can be written as

$$\overline{u_i u_i}^+ = C_q\, \bar{\varepsilon}^{+2/3}\, x_2^{+2/3}, \quad \overline{\theta\theta}^+ = C_\theta\, \bar{\varepsilon}^{+-1/3}\, \bar{\varepsilon}_\theta^+\, x_2^{+2/3}. \tag{4.2a,b}$$

Since $\bar{\varepsilon}^+ \sim \bar{\varepsilon}_\theta^+ \sim 1/x_2^+$ in the overlap region, we can obtain

$$\overline{u_i u_i}^+ \sim \overline{\theta\theta}^+ \sim const. \tag{4.3}$$

Finally, in the viscous-convective range at large Pr, if both $\bar{\varepsilon}^+$ and $\bar{\varepsilon}_\theta^+$ collapse in the same x_2^+ range, then $\overline{\theta\theta}^* = const$ implies that $\overline{\theta\theta}^+ = const\, \theta_B^{+2}$.

All of the analysis above is based on the direct numerical simulations (DNS) data. As pointed out by Smits (2022), over the last two decades or so, there have been major advances in instrumentation, such as the nanoscale thermal anemometry probes developed at Princeton (Kunkel, Arnold & Smits 2006; Bailey *et al.* 2010; Vallikivi *et al.* 2011; Vallikivi & Smits 2014). This has allowed higher Reynolds number experimental data to be obtained, up to $Re_\tau \sim 10^5$, and thus has greatly advanced our understanding of the scaling and structure of wall turbulence. It is hence desirable to examine experimental data in wall flows at higher Reynolds numbers. Figures 18(*a,b*) show the distributions of $\overline{u_1 u_1}^+$ in a pipe and a boundary layer (Vallikivi *et al.* 2011, 2015*b*; Hultmark *et al.* 2012, 2013; Rosenberg *et al.* 2013; Vallikivi, Ganapathisubramani & Smits 2015*a*) – downloaded from https://smits.princeton.edu/data-sets. The corresponding values of the viscous-scaled sensor length $l^+ = l u_\tau / \nu$, where l is the sensor length, are shown in table 1. We can observe that the maximum l^+ is 45.5 in the pipe, and 75 in the boundary layer; $\overline{u_1 u_1}^+$ will therefore be underestimated in the near-wall region (Smits *et al.* 2011*a*). For this reason, a spatial filtering correction, proposed by Smits *et al.* (2011*a*), has been applied to those data. For reference, we add in figures 18(*a,b*) the data of Samie *et al.* (2018) in the boundary layer at $Re_\tau = 6000$–$20\,000$ with $l^+ = 2.4$–3.5, which allows all turbulence scales, including the smallest scales, to be resolved.

The following comments can be made with regard to figure 18.

(i) Smits (2022) concluded that an outer peak in $\overline{u_1 u_1}^+$ emerges at high Re_τ in the pipe and boundary layer, and the inner peak increases with Re_τ, up to $Re_\tau = 20\,000$. Those features are indeed observed in figures 18(*a,b*).

(ii) Based on the analysis in the context of (4.1)–(4.3), there should be an x_2^+ range $\overline{u_1 u_1}^+ \sim const$, which can indeed be observed by some of the distributions in
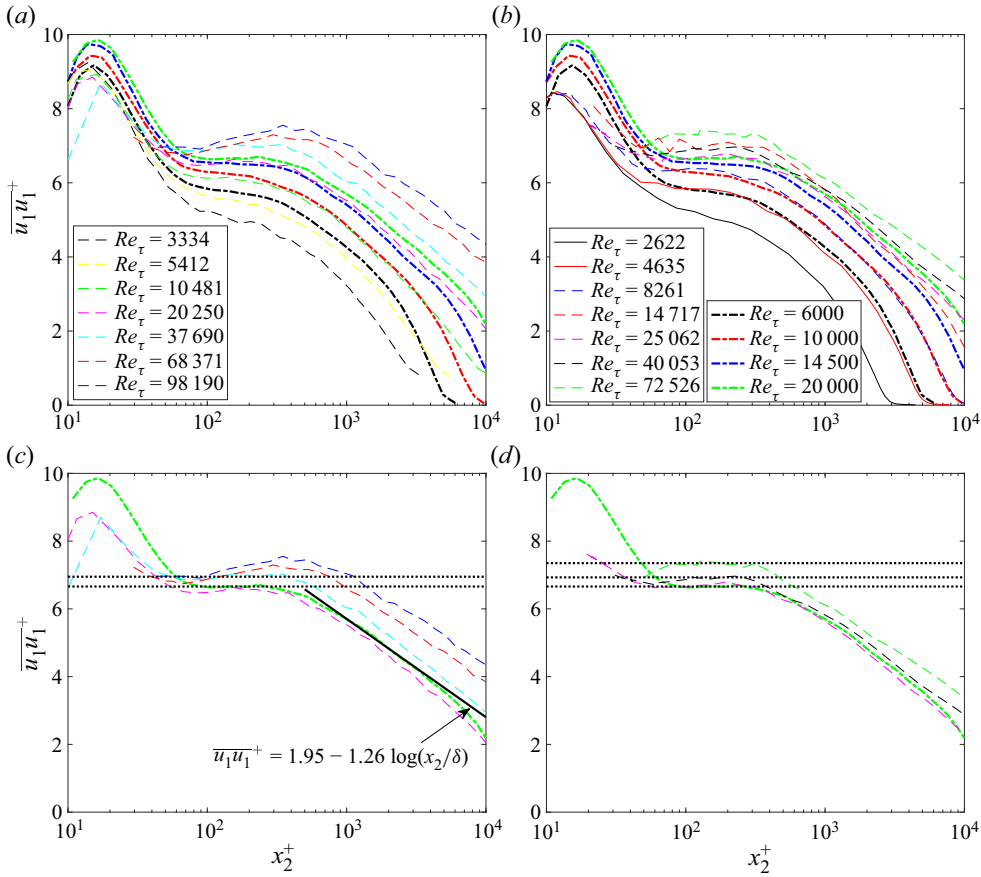
Figure 18. (*a*,*b*) Distributions of $\overline{u_1 u_1}^+$ in a pipe and a boundary layer. Data of Vallikivi *et al.* (2011, 2015*a*,*b*), Hultmark *et al.* (2012, 2013) and Rosenberg *et al.* (2013). Note that the values of the viscous-scaled sensor length $l^+ = l u_\tau / \nu$ at each Re_τ are shown in table 1. For reference, also shown are the data of Samie *et al.* (2018) in a boundary layer at $Re_\tau = 6000$–20 000 with $l^+ = 2.4$–3.5 (thick dashed curves). (*c*,*d*) Distributions of $\overline{u_1 u_1}^+$ corresponding to (*a*,*b*) for only $Re_\tau \gtrsim 20\,000$. The solid line in (*c*) is $\overline{u_1 u_1}^+ = 1.95 - 1.26 \log(x_2/\delta)$. The horizontal dotted lines in (*c*) indicate the values 6.66 and 6.95 respectively. The horizontal dotted lines in (*d*) indicate the values 6.66, 6.93 and 7.35.

Pipe	Re_τ	3334	5412	10 481	20 250	37 690	68 371	98 190
	l^+	3.1	5.0	9.7	18.8	35.0	31.7	45.5
Boundary layer	Re_τ	2622	4635	8261	14 717	25 062	40 053	72 526
	l^+	5.8	10	17	33	29	47	75

Table 1. Values of the viscous-scaled sensor length l^+ corresponding to the data in figures 18(*a*,*b*).

figures 18(*a*,*b*) for $Re_\tau \gtrsim 20\,000$. In order to examine this feature more closely, we report in figures 18(*c*,*d*) the $\overline{u_1 u_1}^+$ distributions corresponding to figures 18(*a*,*b*) for only $Re_\tau \gtrsim 20\,000$. In the boundary layer, there is an approximate plateau at all Re_τ, with values of approximately 6.66, 6.93 and 7.35, over the range $80 \lesssim x_2^+ \lesssim 300$ (except for $Re_\tau = 40\,053$ which has a slightly narrower plateau over the range $100 \lesssim x_2^+ \lesssim 300$),

indicating an emergence of $\overline{u_1u_1}^+ \sim const$ (figure 18d). An approximate plateau, with a value of approximately 6.95, can also be observed in the pipe at $Re_\tau = 37\,690$ over the range $100 \lesssim x_2^+ \lesssim 300$ (figure 18c).

(iii) The boundary layer data of Samie *et al.* (2018) show that $\overline{u_1u_1}^+$ increases systematically with Re_τ for $Re_\tau = 6000$–$20\,000$ at any given x_2^+ (figures 18a,b). However, the magnitude of $\overline{u_1u_1}^+$ at $Re_\tau = 20\,250$ in the pipe is smaller than that in the boundary layer at comparable Re_τ (=20 000) for $x_2^+ \lesssim 100$ (figure 18c). Also, the magnitudes of $\overline{u_1u_1}^+$ at $Re_\tau = 68\,371$–$98\,190$ in the pipe are smaller than or close to that in the boundary layer at $Re_\tau = 20\,000$ for $x_2^+ \lesssim 70$. This may be due to the correction scheme of Smits *et al.* (2011a). Indeed, Samie *et al.* (2018) compared the corrected $\overline{u_1u_1}^+$ distributions ($l^+ = 20$–29), using the scheme proposed by Smits *et al.* (2011a), with the fully resolved $\overline{u_1u_1}^+$ distributions, measured by a nanoscale thermal anemometry probe (NSTAP), for $Re_\tau = 6000$–$20\,000$ (see their figure 9). Their results show that the correction scheme of Smits *et al.* (2011a) performs adequately up to $Re_\tau = 14\,500$; however, at $Re_\tau = 20\,000$ ($l^+ = 29$), the magnitudes of the corrected $\overline{u_1u_1}^+$ distributions slightly underestimated the fully resolved $\overline{u_1u_1}^+$ measured by the NSTAP. It is expected that at given x_2^+ in the near-wall region, this underestimation may increase as Re_τ and l^+ increase.

(iv) As discussed above, figure 18 shows that $\overline{u_1u_1}^+ \sim const$ can be observed for the boundary layer data of Samie *et al.* (2018) over the range $80 \lesssim x_2^+ \lesssim 300$ at $Re_\tau = 20\,000$. If $\bar{\varepsilon} \sim x_2^{-1}$ (or equivalently, $u_K^+ \sim x_2^{-1/4}$) can be observed in the same x_2^+ range, then this would lead to $\overline{u_1u_1}^* \sim x_2^{*2/3}$, the prediction of the present hypothesis. Although figure 17 of Samie *et al.* (2018) shows that u_K^+ and η^+ exhibit reasonable collapse in the range $10 \lesssim x_2^+ \lesssim 500$ for $Re_\tau = 6000$–$20\,000$, there is no discernible range of x_2^+ over which we can observe $u_K^+ \sim x_2^{-1/4}$ or $\eta^+ \sim x_2^{1/4}$. One possible reason is that they assumed local isotropy to estimate the mean turbulent kinetic energy dissipation rate, i.e. $\bar{\varepsilon}_{iso} = 15\nu \int_0^\infty k_x^2 \phi_{u_1}(k_x)\,\mathrm{d}k_x$, which would result in $\bar{\varepsilon}$ being underestimated. As an example, we show in figure 19(a) the $\bar{\varepsilon}_{iso}/\bar{\varepsilon}$ distribution in a channel at comparable Re_τ (=5200–8000). The magnitude of $\bar{\varepsilon}_{iso}/\bar{\varepsilon}$ increases from 0 to 1 when x_2^+ increases from the wall to the region close to the centreline. Interestingly, $\bar{\varepsilon}_{iso}/\bar{\varepsilon}$ appears to be independent of Re_τ at given x_2^+ when $x_2^+ \gtrsim 30$. In order to obtain a more accurate estimation of $\bar{\varepsilon}$ for the data of Samie *et al.* (2018) at $Re_\tau = 20\,000$, we assume that the ratio $\bar{\varepsilon}_{iso}/\bar{\varepsilon}$ for $x_2^+ \gtrsim 30$ in the channel at $Re_\tau = 8000$ also applies to that in a boundary layer at large Re_τ. The u_K^+ distribution, based on the 'new' estimates of $\bar{\varepsilon}$, is shown figure 19(a) (pink curve). Also shown in figure 19(a) is the u_K^+ distribution, based on $\bar{\varepsilon}_{iso}$ of Samie *et al.* (2018) (black curve). It can be observed that the magnitude of u_K^+, based on $\bar{\varepsilon}$, is systematically larger than that based on $\bar{\varepsilon}_{iso}$ when $x_2^+ \lesssim 400$. More importantly, $u_K^+ \sim x_2^{-1/4}$ is satisfied adequately in the range $x_2^+ \lesssim 700$, which will result in $\overline{u_1u_1}^* \sim x_2^{*2/3}$ in the overlap region between $u_K^+ \sim x_2^{-1/4}$ and $\overline{u_1u_1}^+ = const$; this is supported by the distribution in figure 19(b), where we can observe that $\overline{u_1u_1}^* \sim x_2^{*2/3}$ is indeed satisfied approximately over the range $32 \lesssim x_2^* \lesssim 90$. Note that at $Re_\tau = 20\,000$, $x_2^* = 32$ and 90 correspond to $x_2^+ = 79$ and 312, respectively. For reference, also shown in figure 19(b) is the $\overline{u_1u_1}^*$ distribution of Hoyas *et al.* (2022) in a channel at $Re_\tau = 10^4$. It is worth mentioning that $\overline{u_1u_1}^* \sim x_2^{*2/3}$ in the range $35 \lesssim x_2^* \lesssim 70$ for the channel data. This is consistent with the local slope shown in figure 11.
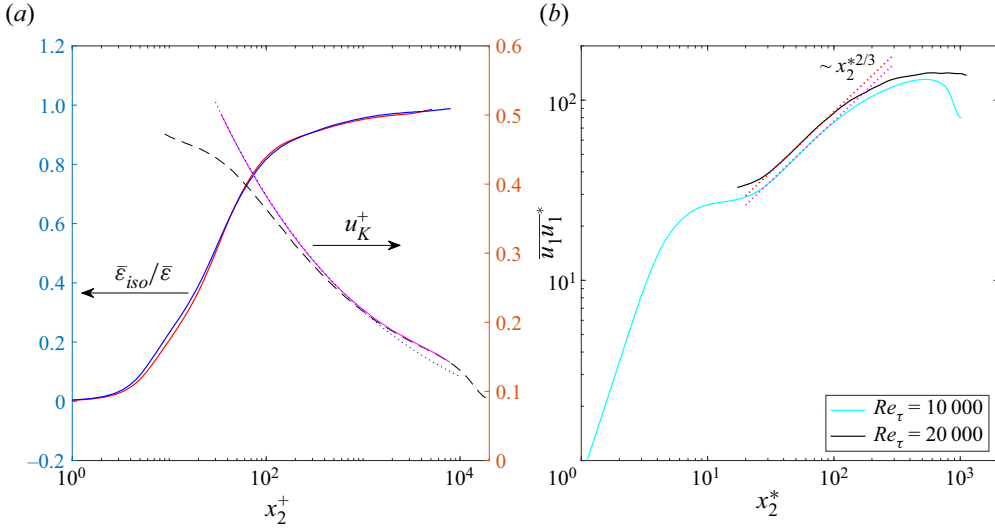
Figure 19. (a) On the left, distributions of $\bar{\varepsilon}_{iso}/\bar{\varepsilon}$ in a channel at $Re_\tau = 5200$ (red curve) and $Re_\tau = 8000$ (blue curve); data of Lee & Moser (2015, 2019) and Kaneda & Yamamoto (2021). On the right, distributions of u_K^+ based on $\bar{\varepsilon}_{iso}$ (black curve, which is reproduced from figure 17(b) of Samie *et al.* 2018) and $\bar{\varepsilon}$ (pink curve) in a boundary layer at $Re_\tau = 20\,000$ (see text). Dotted curve is $0.46x_2^{+-1/4}$. (b) Distributions of $\overline{u_1u_1}^*$ ($= \overline{u_1u_1}^+/u_K^{+2}$) in a boundary layer at $Re_\tau = 20\,000$ (see text). For reference, also shown as a cyan curve is the $\overline{u_1u_1}^*$ distribution of Hoyas *et al.* (2022) in a channel at $Re_\tau = 10^4$. Dotted curve is $\sim x_2^{*2/3}$.

(v) We recall that the attached eddy hypothesis proposed by Townsend (1976) predicts

$$\overline{u_1u_1}^+ = B_1 - A_1 \log(x_2/\delta), \tag{4.4}$$

where B_1 and A_1 are constants. Equation (4.4) has been supported strongly by both the experimental and numerical data at high Re_τ (see the review of Marusic & Monty 2019). We add the distribution of (4.4) in figure 18(c) with $B_1 = 1.95$ and $A_1 = 1.26$ (Samie *et al.* 2018). It is interesting that (4.4) predicted by the attached eddy hypothesis, and the present prediction $\overline{u_1u_1}^+ \sim const$, are located in different x_2^+ ranges at $Re_\tau = 20\,000$. Namely, (4.4) and $\overline{u_1u_1}^+ \sim const$ can co-exist.

5. Relationship to the scaling of small-scale wall turbulence

We recall that Tang & Antonia (2022) have shown that an overall feature of the Kolmogorov-normalized energy spectra $\phi_{u_1}(k_{x_3}^*)$, $\phi_{u_2}(k_{x_3}^*)$ and $\phi_{u_3}(k_{x_3}^*)$ is that their collapse extends to increasingly smaller wavenumbers (larger scales) with increasing Re_τ. Rather than discussing the behaviour of $\phi_{u_1}(k_{x_3}^*)$, $\phi_{u_2}(k_{x_3}^*)$ and $\phi_{u_3}(k_{x_3}^*)$, we focus here on the second-order velocity structure function $\overline{(\delta u_i)^2}(r_z^*)$, which is closely related to $\phi_{u_1}(k_{x_3}^*)$, $\phi_{u_2}(k_{x_3}^*)$ and $\phi_{u_3}(k_{x_3}^*)$ since (e.g. Dickey & Mellor 1979; Monin & Yaglom 2007)

$$\overline{(\delta u_i)^2}(r_z^*) = 2 \int_0^\infty \phi_{u_i}(k_z^*) \left(1 - \cos(k_z^* r_z^*)\right) dk_z^*, \tag{5.1}$$

where r_z is the separation between two points in the x_3 direction; note that the repeated index i does not indicate summation in (5.1a,b) since we are interested in the behaviour
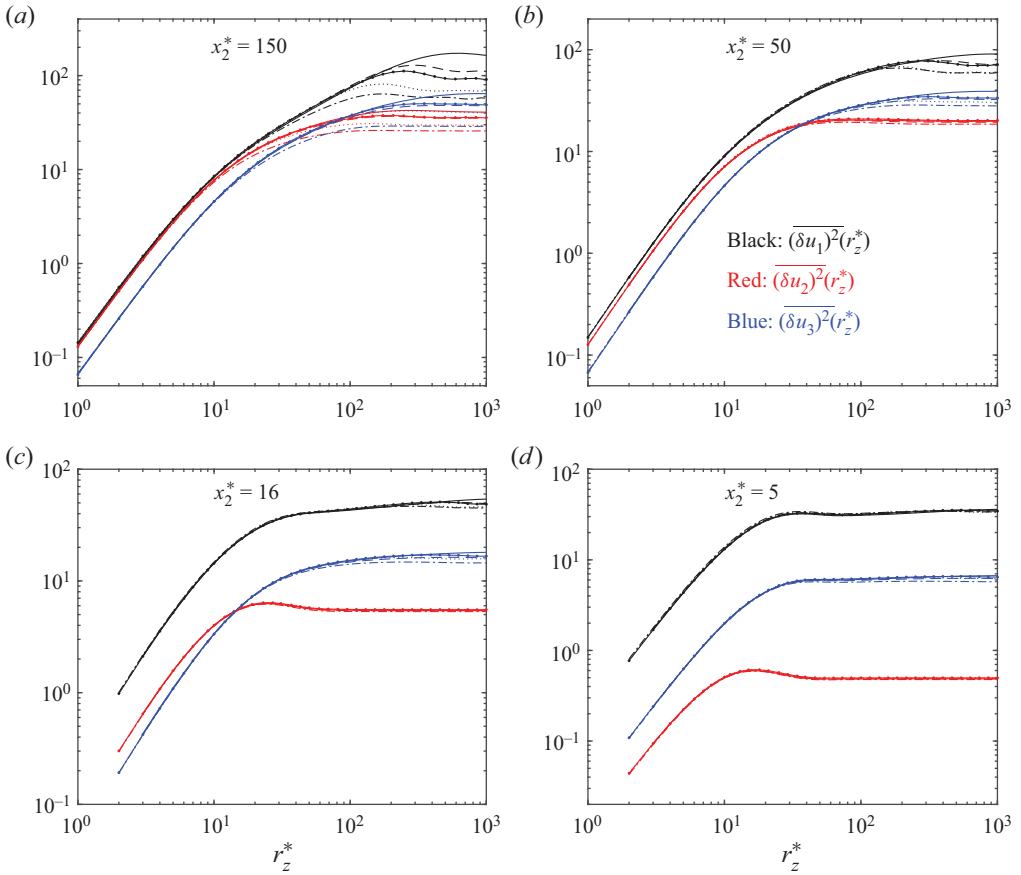
Figure 20. Kolmogorov-normalized second-order structure function $\overline{(\delta u_i)^2}(r_z^*)$ at $x_2^* = 5$, 16, 50 and 150. Dotted and solid/dotted curves correspond to the boundary layer data at $Re_\tau = 1307$ and 1988, respectively. Dash-dotted, dashed and solid curves correspond to the channel data at $Re_\tau = 1000$, 2000 and 5200, respectively. Note that as in figure 8, only the data for $Re_\tau \geq 1000$ are shown.

of different components. Equation (5.1a,b) is obtained based on the relation $\overline{(\delta u_i)^2}(r_z) = 2(\overline{u_i^2} - \overline{u_i u_i'}) = 2[\int_0^\infty \phi_{u_i}(k_z)\, dk_z - \int_0^\infty \phi_{u_i}(k_z) \cos(k_z r_z)\, dk_z]$ (e.g. Dickey & Mellor 1979). The advantage of $\overline{(\delta u_i)^2}(r_z^*)$ is that it leads to $2\overline{u_1^{*2}}$, $2\overline{u_2^{*2}}$ and $2\overline{u_3^{*2}}$ as $r_z^* \to L^*$ (where L is the integral scale). We select four typical locations, i.e. $x_2^* = 5$, 16, 50 and 150. The minimum r_z^* at different locations is calculated based on the Kolmogorov-normalized resolution of the mesh in the x_3 direction. Note that when data were not obtained at exactly $x_2^* = 5$, 16, 50 and 150, interpolation was used, based on available spectra closest to these locations. Then $\overline{(\delta u_i)^2}(r_z^*)$ is calculated based on (5.1a,b). Figures 20(a–d) show the distributions of $\overline{(\delta u_i)^2}(r_z^*)$ at $x_2^* = 150$, 50, 16 and 5, respectively.

The following comments can be made with regard to figure 20.

(i) Local isotropy requires $\overline{(\delta u_1)^2}(r_z^*) = \overline{(\delta u_2)^2}(r_z^*)$. There is a strong departure from local isotropy at $x_2^* = 5$ and 16 in the scale range $r_z^* \lesssim 10$. The departure gradually
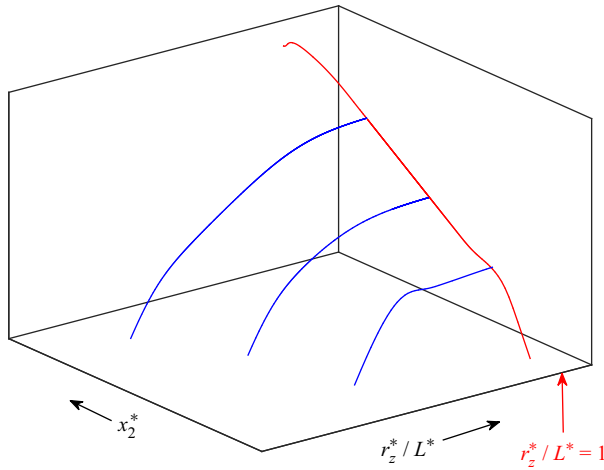
960 A18-22

Figure 21. Sketch of $\overline{u_i^{*2}}$ versus x_2^* (red curve) and $\overline{(\delta u_i)^2}(r_z^*)/2$ versus r_z^*/L^* (blue curves) on log–log scales. The red arrow corresponds to the location $r_z^*/L^* = 1$. Note that $\overline{(\delta u_i)^2}(r_z^*)/2$ reaches $\overline{u_i^{*2}}$ as r_z^*/L^* approaches 1.

decreases as x_2^* increases, and appears to be negligible at $x_2^* = 150$, suggesting an approach towards local isotropy in the context of $\overline{(\delta u_1)^2}(r_z^*) = \overline{(\delta u_2)^2}(r_z^*)$.

(ii) At $x_2^* = 5$, $\overline{(\delta u_1)^2}(r_z^*)$ and $\overline{(\delta u_2)^2}(r_z^*)$ collapse at all r_z^*, whereas $\overline{(\delta u_3)^2}(r_z^*)$ appears to collapse only for $r_z^* \lesssim 30$. Consequently, the degree of collapse is better for $\overline{u_1^{*2}}$ and $\overline{u_2^{*2}}$ than for $\overline{u_3^{*2}}$.

(iii) At $x_2^* = 16$, only $\overline{(\delta u_2)^2}(r_z^*)$ collapses at all r_z^*. An important feature of the other distributions is that at a given x_2^*, the collapse extends to increasingly larger scales with increasing Re_τ. One thus expects that as Re_τ is increased to a sufficiently large value, the collapse would extend to all r_z^*. In this situation, the sketch of the predictions for $\overline{u_i^{*2}}$ shown in figure 2 can be further extended to the r_z^* direction, which is shown in figure 21. Note that r_z^* has been divided by a Kolmogorov-normalized integral scale L^* so that $\overline{(\delta u_i)^2}(r_z^*)/2$ leads to $\overline{u_i^{*2}}$ as $r_z^*/L^* \to 1$ (or equivalently, $r_z/L \to 1$). For clarity, distributions of $\overline{(\delta u_i)^2}(r_z^*)/2$ for only three values of x_2^* are shown. We emphasize that as $r_z^*/L^* \to 1$ and $x_2^* \to \delta^*$ (sufficiently far away from the wall), $\overline{(\delta u_i)^2}(r_z^*)/2$ should go to ∞ as $Re_\tau \to \infty$. However, $\overline{(\delta u_i)^2}(r_z^*)/2$ should be independent of the Reynolds number both in the region $x_2^* \ll \delta^*$ (including all scales) and in the scale range $r_z^*/L^* \ll 1$ as $x_2^* \to \delta^*$, as $Re_\tau \to \infty$; the latter corresponds to the prediction of the classical hypotheses of Kolmogorov (1941). Although not discussed here, the same remark can be made with regard to $\overline{(\delta u_i)^2}(r_x^*)/2$ and the scalar structure function $\overline{(\delta\theta)^2}/2$ in both the r_x^* and r_z^* directions.

Further, the collapse of $x_2^+ \bar{\varepsilon}^+$ distributions in the boundary layer (figure 14b) in the range $10 \lesssim x_2^+ \lesssim 30$ implies that the wall parameters and the Kolmogorov scales can be used interchangeably for quantities such as the energy spectra and the second-order velocity structure function in the same x_2^+ range. Indeed, Samie *et al.* (2018) have shown that the wall-parameter-normalized premultiplied energy spectra at $x_2^+ = 15$ and 24, 92, 178 and

277 collapse reasonably well for the small wavelength ranges in the boundary layer at $Re_\tau = 6000$, $10\,000$, $14\,500$ and $20\,000$, respectively; the collapse of the premultiplied energy spectra extends to larger x_2^+, up to 277, suggesting that the $\bar{\varepsilon}^+$ distributions for $Re_\tau \gtrsim 6000$ in the boundary layer have extended to at least $x_2^+ \approx 277$. This can be inferred from figure 17 of Samie *et al.* (2018), which shows that the wall-parameter-normalized Kolmogorov length and velocity scales (the energy dissipation rate was estimated by integrating the one-dimensional streamwise dissipation spectrum) exhibit reasonable collapse in the range $10 \lesssim x_2^+ \lesssim 500$.

6. Exploratory predictions for high-order moments at all scales

The predictions of the present hypothesis can be extended to high-order moments. For simplicity, we consider only the velocity and passive scalar statistics $\overline{u_i^n}^*$ and $\overline{\theta^n}^*$ for $n \geq 3$, which can be expressed as

$$\overline{u_i^n}^* = f_n(x_2^*), \quad \overline{\theta^n}^* = f_{\theta n}(x_2^*), \tag{6.1a,b}$$

where the functions f_n and $f_{\theta n}$ are independent of the Reynolds and Péclet numbers once appropriate values of the Reynolds and Péclet numbers are reached. In the inertial-convective range $0 \ll x_2^* \ll \delta^*$,

$$\overline{u_i^n}^* = C_n x_2^{*n/3}, \quad \overline{\theta^n}^* = C_{\theta n} x_2^{*n/3}. \tag{6.2a,b}$$

Finally, at large Pr, there exists a viscous-convective range for $\overline{\theta^n}^*$ between the inertial-convective and the viscous-diffusion ranges over which

$$\overline{\theta^n}^* = const. \tag{6.3}$$

Combining all predictions of the present hypothesis with those of the small-scale wall turbulence hypothesis proposed by Tang & Antonia (2022), we can formulate a more complete hypothesis for turbulent statistics in wall turbulence, as follows.

In wall turbulence at sufficiently high Reynolds and Péclet numbers, except for the large-scale quantities in the region far away from the wall, all turbulent statistics are independent of the Reynolds and Péclet numbers when the normalization uses $\bar{\varepsilon}$, $\bar{\varepsilon}_\theta$ and ν. They depend only on the turbulent scale (or wavenumber) and the distance from the wall. The larger the Reynolds and Péclet numbers, the larger the distance from the wall and the range of turbulent scales over which this hypothesis applies. In particular, there exist two inertial-convective ranges over which the scaling parameters are $\bar{\varepsilon}$ and $\bar{\varepsilon}_\theta$, and two viscous-convective ranges (at large Pr) over which the effect of ν is important. For large-scale quantities such as $\overline{u_i^n}^*$ and $\overline{\theta^n}^*$, the inertial-convective range is located in the region $0 \ll x_2^* \ll \delta^*$. The other pertains to the small-scale quantities and is located in the region $0 \ll r^* \ll L^*$ as $x_2^* \to \delta^*$. Also, there are two viscous-convective ranges for the scalar variance and the scalar structure function, located between the viscous-diffusive and inertial-convective ranges.

The predictions of the above complete hypothesis are sketched in figure 22, which shows the approximate locations and scale ranges over which the scaling based on $\bar{\varepsilon}$, $\bar{\varepsilon}_\theta$ and ν is tenable. We recall that figure 21 is for the second-order velocity structure function $\overline{(\delta u_i)^2}(r_z^*)$, whereas figure 22 is for any quantity (which can be a function of the turbulent scale r^* and x_2^*). If we focus on the quantity $\overline{(\delta u_i)^2}(r_z^*)$, then figure 22 can be considered, at least approximately, as the projection of the three-dimensional plot of figure 21 onto the
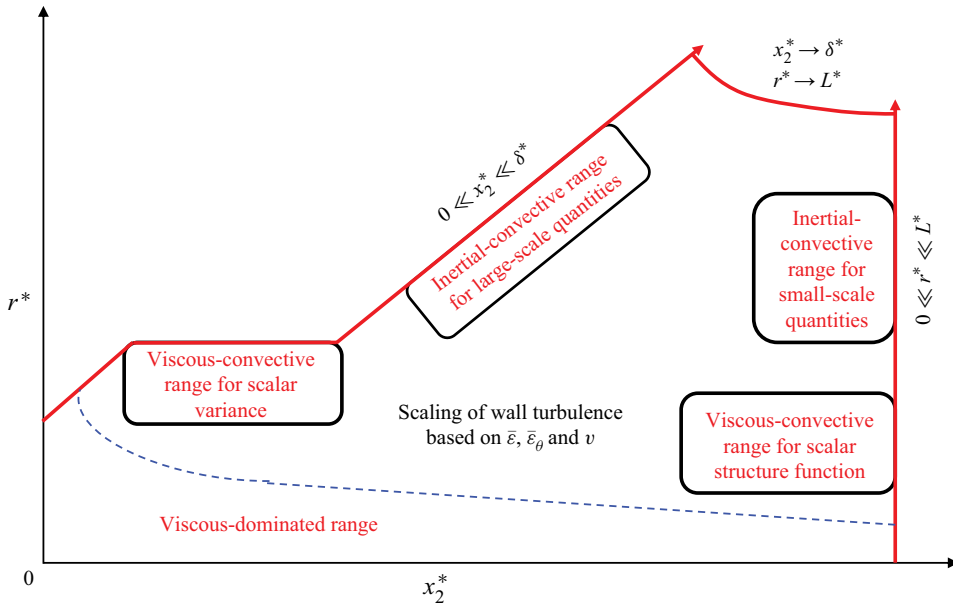
Figure 22. Summary of predictions, based on the present hypothesis, for turbulent statistics in wall turbulence when the normalization uses $\bar{\varepsilon}$, $\bar{\varepsilon}_\theta$ and ν at sufficiently high Reynolds number. The red line is the upper limit for x_2^* and r^* over which the scaling based on $\bar{\varepsilon}$, $\bar{\varepsilon}_\theta$ and ν holds. Note that the two viscous-convective ranges apply only to the passive scalar at large Pr. Note also that the present scaling does not apply in the region $x_2^* \to \delta^*$ and $r^* \to L^*$. The dashed curve is the upper limit of the viscous-dominated range. Here, r can be either r_x or r_z.

r_z^*–x_2^* plane, after r_z^*/L^* in figure 21 is multiplied by L^*. We believe that the predictions in figure 22 could be one possible ultimate statistical state of wall turbulence. It is evident that this complete hypothesis for wall turbulence needs to be tested against data, especially for moments of order higher than 2, in future investigations.

Finally, we stress that as $Re_\tau \to \infty$, if both $\bar{\varepsilon}^+$ and $\bar{\varepsilon}_\theta^+$ collapse onto unique curves at all locations in the range $x_2^+ \lesssim x_{2\alpha}^+$ in all wall flows, then the wall parameters and the scaling parameters $\bar{\varepsilon}$, $\bar{\varepsilon}_\theta$ and ν can be used interchangeably in the same x_2^+ range. In this case, the scaling of wall turbulence based on wall parameters should also be tenable in the range $x_2^+ \lesssim x_{2\alpha}^+$ (figure 23), which shows the approximate locations over which the scaling based on wall parameters is tenable. This is consistent with the perspective of Chen & Sreenivasan (2022) whereby wall-parameter-normalized statistics displaying non-zero wall values or near-wall peaks may become bounded at infinitely large Reynolds numbers. In particular, in the overlap region between $\bar{\varepsilon} \sim \bar{\varepsilon}_\theta \sim x_2^{-1}$ and the inertial-convective range for large-scale quantities such as $\overline{u_i^n}^*$ and $\overline{\theta^n}^*$, wall-parameter-normalized large-scale quantities should approach constant values, as indicated in figure 23. We can demonstrate this by using $\overline{u_i^n}^*$ as an example, i.e.

$$\overline{u_i^n}^* = C_n x_2^{*n/3} = \frac{\overline{u_i^n}^+}{u_K^{+n}} = C_n (x_2^+ u_K^+)^{n/3}$$

$$\Rightarrow \overline{u_i^n}^+ = C_n x_2^{+n/3} u_K^{+4n/3} = C_n x_2^{+n/3} \bar{\varepsilon}^{+n/3} \sim C_n. \tag{6.4}$$
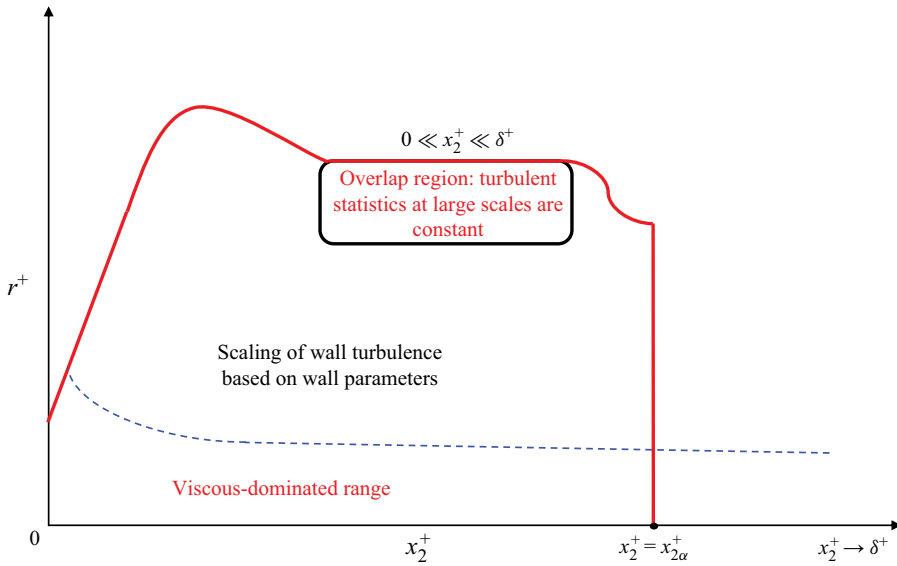
960 A18-25

Figure 23. Summary of predictions for turbulent statistics in wall turbulence in the range $x_2^+ \lesssim x_{2\alpha}^+$ when the normalization uses wall parameters at sufficiently high Reynolds number. The red line is the upper limit for x_2^+ and r^+ over which the scaling based on wall parameters holds. Note that this scaling requires both $\bar{\varepsilon}^+$ and $\bar{\varepsilon}_\theta^+$ to collapse onto unique curves at all locations in the range $x_2^+ \lesssim x_{2\alpha}^+$, and does not apply in the region $x_2^+ > x_{2\alpha}^+$. The dashed curve is the upper limit of the viscous-dominated range. Here, r can be either r_x or r_z.

We expect that a wall-parameter-based scaling could be another possible ultimate statistical state of wall turbulence. Again, this needs to be tested in the future.

We recall that a region where $\overline{u_1 u_1}^+ \sim const$ can be observed in some of the distributions in figures 18(c,d) for $Re_\tau \gtrsim 20\,000$. However, the magnitude of the constant continues to depend on Re_τ. This implies that a value of Re_τ, even when equal to $72\,526$ (in figure 18d), may not be 'sufficiently high' for $\overline{u_i u_i}^+ = const$ (independently of Re_τ) to be established unequivocally. In order to demonstrate this further, we now focus on the behaviour of $-\overline{u_1 u_2}^+$ at large Re_τ. A well-known relation for the total shear stress in the channel is

$$\tau_w \left(1 - \frac{x_2}{\delta}\right) = \rho \nu \frac{d\bar{U}_1}{dx_2} - \rho \overline{u_1 u_2}, \tag{6.5}$$

which, after trivial manipulations, can be rewritten as

$$-\overline{u_1 u_2}^+ = 1 - \frac{x_2^+}{Re_\tau} - \frac{d\bar{U}_1^+}{dx_2^+}. \tag{6.6}$$

If we focus on the region away from the wall and channel centreline, then $d\bar{U}_1^+/dx_2^+$ may be replaced with the log-law region, i.e.

$$-\overline{u_1 u_2}^+ = 1 - \frac{x_2^+}{Re_\tau} - \frac{1}{\kappa x_2^+}. \tag{6.7}$$

Smits (2022) concluded that $\kappa = 0.40 \pm 0.02$ based on a large amount of data measured in the Princeton SuperPipe using both Pitot tubes and hot wires. Figure 24(a) shows the
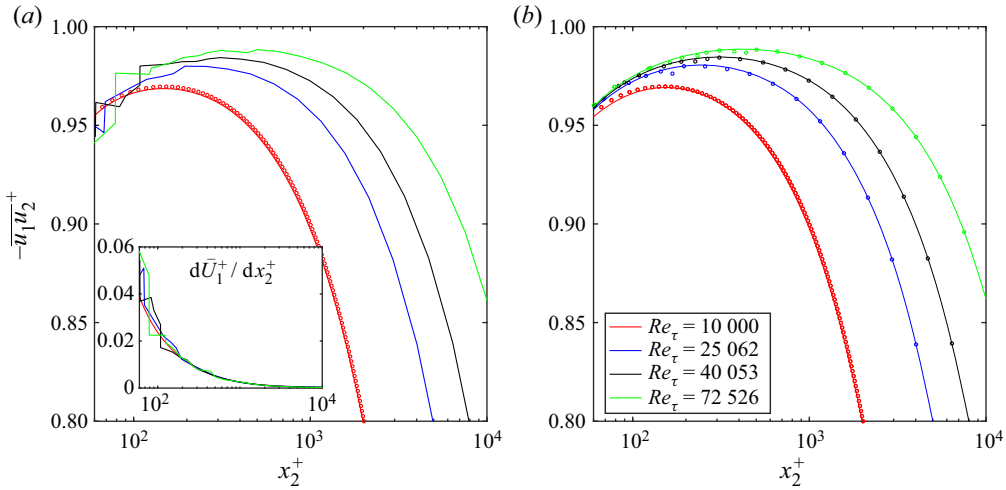
960 A18-26

Figure 24. (*a*) Distributions of $-\overline{u_1 u_2}^+$ (curves) based on (6.6) at $Re_\tau = 10^4$, 25 062, 40 053 and 72 526. Note that the calculation of (6.6) is based on the DNS data of $d\bar{U}_1^+/dx_2^+$ in a channel at $Re_\tau = 10^4$ (Hoyas *et al.* 2022) and the experimental data at $Re_\tau = 25\,062$–72 526 (Vallikivi *et al.* 2011, 2015*a,b*; Hultmark *et al.* 2012, 2013; Rosenberg *et al.* 2013), respectively (see the inset). (*b*) Distributions of $-\overline{u_1 u_2}^+$ (curves) based on (6.7) with $\kappa = 0.42$ (Smits 2022) at $Re_\tau = 10^4$, 25 062, 40 053 and 72 526. Also shown are the calculations based on (6.6) at $Re_\tau = 25\,062$ (○, blue), 40 053 (○) and 72 526 (○, green), after replacing $d\bar{U}_1^+/dx_2^+$ in the range $x_2^+ < 150$ with the DNS data of Hoyas *et al.* (2022) (see text). For comparison, also shown in (*a,b*) is the $-\overline{u_1 u_2}^+$ distribution (○, red) of Hoyas *et al.* (2022) at $Re_\tau = 10^4$.

distributions of $-\overline{u_1 u_2}^+$ based on (6.6) at $Re_\tau = 10^4$, 25 062, 40 053 and 72 526. To plot (6.6), we used the DNS data of $d\bar{U}_1^+/dx_2^+$ at $Re_\tau = 10^4$ in a channel (Hoyas *et al.* 2022) and the experimental data at $Re_\tau = 25\,062$–72 526 in a boundary layer (Vallikivi *et al.* 2011, 2015*a,b*; Hultmark *et al.* 2012, 2013; Rosenberg *et al.* 2013), respectively; they are shown in the inset. The use of $d\bar{U}_1^+/dx_2^+$ in a boundary layer should be reasonable since it is well-accepted that $\bar{U}_1^+$ is universal in the inner layer of wall flows. Values $Re_\tau = 25\,062$, 40 053 and 72 526 correspond to the three largest values of Re_τ in figures 18(*b,d*). We can observe that the variation of $-\overline{u_1 u_2}^+$ with Re_τ is systematic in the region $x_2^+ \gtrsim 150$. In the range $x_2^+ < 150$, the distributions at $Re_\tau = 25\,062$–72 526 exhibit some scatter. This reflects the scatter of $d\bar{U}_1^+/dx_2^+$ in the same x_2^+ range (see the inset). Figure 24(*b*) shows the distributions of $-\overline{u_1 u_2}^+$ based on (6.7) with $\kappa = 0.42$ (Smits 2022) at the same Re_τ as in figure 24(*a*). Also shown are the distributions based on (6.6) at $Re_\tau = 25\,062$–72 526, after replacing $d\bar{U}_1^+/dx_2^+$ in the range $x_2^+ < 150$ with the DNS data of Hoyas *et al.* (2022) at $Re_\tau = 10^4$. There is adequate agreement between (6.6) and (6.7). Finally, the $-\overline{u_1 u_2}^+$ distribution of Hoyas *et al.* (2022) at $Re_\tau = 10^4$ is shown in figures 24(*a,b*). It agrees reasonably well with (6.6) and (6.7). It is evident that even at $Re_\tau = 72\,526$, $-\overline{u_1 u_2}^+ = 1$ is not established (figure 24). We next quantify, albeit approximately, the values of Re_τ required for $-\overline{u_1 u_2}^+ = 1$ to be established. Figure 25 shows the distributions of $-\overline{u_1 u_2}^+$, based on (6.7) with $\kappa = 0.42$ (Smits 2022), at $Re_\tau = 10^4$, 10^5 and 10^6. It appears that $Re_\tau \sim 10^6$ is needed for $-\overline{u_1 u_2}^+ \approx 1$ to be established in an x_2^+ range of approximately two decades ($2 \times 10^2 \lesssim x_2^+ \lesssim 10^4$).
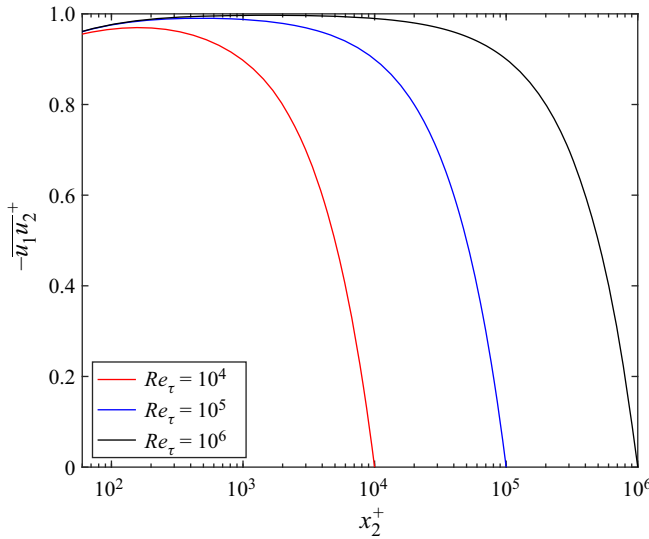
Figure 25. Distributions of $-\overline{u_1 u_2}^+$ based on (6.7) with $\kappa = 0.42$ (Smits 2022) at $Re_\tau = 10^4$, 10^5 and 10^6.

7. Concluding remarks

In summary, a hypothesis has been proposed to describe the behaviour of the Reynolds stresses, turbulent kinetic energy and scalar variance in wall turbulence. The major conclusions can be summarized as follows.

(i) When the normalization is based on $\bar{\varepsilon}$, $\bar{\varepsilon}_\theta$ and ν, the independence on the Reynolds and Péclet numbers predicted by the present hypothesis is first satisfied at very small x_2^* before gradually extending to larger x_2^* as Re_τ increases.

(ii) At large but not infinitely large x_2^*, the magnitudes of the Kolmogorov-normalized Reynolds stresses and turbulent kinetic energy depend on Re_τ. Further, the scalar variance, when normalized by $\bar{\varepsilon}$, $\bar{\varepsilon}_\theta$ and ν, depends not only on Re_τ at a given Pr, but also on the Péclet number $Re_\tau Pr$ at a given Re_τ. The normalized quantities vary with Re_τ and $Re_\tau Pr$ systematically, suggesting the importance of the finite Re_τ and $Re_\tau Pr$ effects in the context of establishing the inertial-convective range, i.e. the emergence of the 2/3 power-law scaling. Although independence from the Reynolds and Péclet numbers of those quantities has not yet been observed in the present Re_τ ($\leq 10^4$) and Pr (≤ 7) ranges at moderate x_2^*, a trend towards a 2/3 power-law scaling is discernible for some quantities, such as the turbulent kinetic energy, and the streamwise and wall-normal components of the Reynolds stresses.

(iii) At the highest Pr ($= 7$), there is a trend towards a plateau for the scalar variance when normalized with $\bar{\varepsilon}$, $\bar{\varepsilon}_\theta$ and ν. The plateau falls between the inertial-convective and viscous-diffusive ranges for $Re_\tau = 500$–2000, suggesting an emergence of a viscous-convective range.

The relationship between the wall-parameter normalization and the normalization based on $\bar{\varepsilon}$, $\bar{\varepsilon}_\theta$ and ν has been discussed in the context of $\bar{\varepsilon}^+$ and $\bar{\varepsilon}_\theta^+$. At finite Re_λ and $Pr Re_\lambda$, the scaling based on $\bar{\varepsilon}$, $\bar{\varepsilon}_\theta$ and ν is superior to that based on wall parameters in the context of $\overline{u_i u_j}$, $\overline{u_i u_i}$ and $\overline{\theta\theta}$. We should stress that if the collapse of the distributions of $\bar{\varepsilon}^+$ and $\bar{\varepsilon}_\theta^+$ in wall flows extends to the wall, then both the wall parameters and scaling parameters $\bar{\varepsilon}$, $\bar{\varepsilon}_\theta$ and ν can be used interchangeably in the near-wall region in the context of the Reynolds stresses, turbulent kinetic energy, scalar variance, mean velocity and mean scalar; this may

require $Re_\lambda \to \infty$. In particular, as $Re_\lambda \to \infty$, there should be an overlap range (far away from the wall) over which both $-\overline{u_1 u_2}^+ = 1$ and $\overline{u_1 u_2}^* = C_{12} x_2^{*2/3}$ (inertial-convective range) are established unequivocally, and $\bar{\varepsilon}^+$ collapses perfectly. Further, in this overlap range, $\overline{u_1 u_1}^+$, $\overline{u_2 u_2}^+$, $\overline{u_3 u_3}^+$, $\overline{u_i u_i}^+$ and $\overline{\theta\theta}^+$ should be constant. In the viscous-convective range at large Pr, it is expected that $\overline{\theta\theta}^+ = const\, \theta_B^{+2}$, when both $\bar{\varepsilon}^+$ and $\bar{\varepsilon}_\theta^+$ collapse in the same x_2^+ range.

Finally, the main message of figure 20 is that in the wall region, the Re_τ independence of $\overline{(\delta u_i)^2}(r_z^*)$ is first established at all locations for small scales, and extends to increasingly larger scales with increasing Re_τ. In the region very near the wall, this Re_τ independence can extend to all scales and to increasingly larger values of x_2^* with increasing Re_τ; in the Re_τ range for the currently available data, the x_2^* range over which $\overline{(\delta u_i)^2}(r_z^*)$ collapses depends on the specific quantity investigated. As $Re_\tau \to \infty$, $\overline{(\delta u_i)^2}(r_z^*)$ should be Re_τ-independent both in the near-wall region $x_2^* \ll \delta^*$ (at all scales) and in the small-scale range $r_z^*/L^* \ll 1$ as $x_2^* \to \delta^*$. This picture leads to one possible ultimate statistical state of wall turbulence in the context of the second-order velocity structure function (figure 21). Conceptual summary sketches of the predictions of the present hypothesis, combined with those of the small-scale wall turbulence hypothesis (Tang & Antonia 2022), are given in figure 22 when the normalization is based on $\bar{\varepsilon}$, $\bar{\varepsilon}_\theta$ and ν, and in figure 23 when the normalization uses wall parameters. The latter is consistent with the restoration of wall scaling at asymptotically high Re_τ (Chen & Sreenivasan 2021, 2022). Finally, we should stress that large-scale turbulent statistics, normalized by wall parameters, are approximately constant over the range $0 \ll x_2^+ \ll \delta^+$ (figure 23). This requires $\bar{\varepsilon} \sim \bar{\varepsilon}_\theta \sim x_2^{-1}$.

Declaration of interests. The authors report no conflict of interest.

Author ORCIDs.
 S.L. Tang https://orcid.org/0000-0001-6379-8505.

Appendix A. Dimensional analysis for $\overline{u_i u_i}$ and $\overline{\theta\theta}$ in the range $0 \ll x_2^* \ll \delta^*$

According to the present hypothesis, at a sufficiently, though not infinitely, large distance from the wall ($0 \ll x_2^* \ll \delta^*$), $\overline{u_i u_i}$ and $\overline{\theta\theta}$ should depend only on $\bar{\varepsilon}$ and $\bar{\varepsilon}_\theta$, i.e.

$$\overline{u_i u_i} = f(\bar{\varepsilon}, x_2), \quad \overline{\theta\theta} = g(\bar{\varepsilon}_\theta, x_2). \tag{A1a,b}$$

Application of the Π theorem leads to

$$\overline{u_i u_i} = C_q \bar{\varepsilon}^{\alpha_1} x_2^{\alpha_2}, \quad \overline{\theta\theta} = C_\theta \bar{\varepsilon}^{\alpha_3} \bar{\varepsilon}_\theta^{\alpha_4} x_2^{\alpha_5}, \tag{A2a,b}$$

where C_q and C_θ are constants. Therefore, we obtain

$$L^2 T^{-2} \sim L^{\alpha_2} L^{2\alpha_1} T^{-3\alpha_1}, \quad Q^2 \sim Q^{2\alpha_4} L^{\alpha_5} L^{2\alpha_3} T^{-3\alpha_3} T^{-\alpha_4}, \tag{A3a,b}$$

therefore $\alpha_1 = \alpha_2 = 2/3$ and $\alpha_3 = -1/3$, $\alpha_4 = 1$, $\alpha_5 = 2/3$. $\tag{A4a,b}$

The two equations in (A2a,b) can finally be written as

$$\overline{u_i u_i} = C_q (\bar{\varepsilon} x_2)^{2/3}, \quad \text{or} \quad \overline{u_i u_i}^* = C_q x_2^{*2/3}, \tag{A5}$$

$$\overline{\theta\theta} = C_\theta \bar{\varepsilon}^{-1/3} \bar{\varepsilon}_\theta x_2^{2/3}, \quad \text{or} \quad \overline{\theta\theta}^* = C_\theta x_2^{*2/3}. \tag{A6}$$

Appendix B. Transport equations for $\overline{u_i u_i}$ in the range $40 \leq x_2^+ \leq 200$

We have explained why the scaling based on $\bar{\varepsilon}$, $\bar{\varepsilon}_\theta$ and ν is superior to that based on wall parameters in the near-wall region; see the discussion in the context of (2.3a,b) and (2.4a,b), which are the transport equations for the turbulent kinetic energy $\overline{u_i u_i}$ and the scalar variance $\overline{\theta\theta}$, respectively, in the near-wall region. We now discuss why the present scaling is superior to the wall scaling further away from the wall. For convenience, the discussion here is in the context of the transport equations for $\overline{u_i u_i}$. Figure 26(a) shows all terms in (2.1), i.e. the transport equations for $\overline{u_i u_i}$, after normalizing by wall parameters, in the region $40 \leq x_2^+ \leq 200$. We can observe that (2.1) can be approximately simplified to

$$-\overline{u_1 u_2}^+ \frac{\partial \bar{U}_1^+}{\partial x_2^+} \approx \bar{\varepsilon}^+. \tag{B1}$$

Although not shown here, the ratio $-\overline{u_1 u_2}^+ (\partial \bar{U}_1^+ / \partial x_2^+)/\bar{\varepsilon}$ is in the range 0.91–1.11 for $40 \leq x_2^+ \leq 200$ at $Re_\tau = 10^4$. Namely, (B1) is satisfied within approximately 10 %. We can observe from figure 26(a) that the variation of the wall-parameter-normalized P_U and D terms with Re_τ is systematic at all x_2^+, except for the D term when $Re_\tau \geq 5200$. However, after normalizing (B1) by $\bar{\varepsilon}$ and ν, we obtain

$$-\overline{u_1 u_2}^* \frac{\partial \bar{U}_1^*}{\partial x_2^*} \approx \bar{\varepsilon}^* = 1. \tag{B2}$$

The behaviour of $\bar{U}_1^*$ has been discussed in the context of figure 17. Briefly, $\bar{U}_1^*$ for $Re_\tau \gtrsim 2000$ appears to collapse for $x_2^* \gtrsim 11$, and the larger Re_τ, the wider the x_2^* range over which $\bar{U}_1^*$ is Re_τ-independent (see the discussion of figure 17c). Therefore, (B2) implies that $-\overline{u_1 u_2}^*$ should collapse at large Re_τ and large x_2^*. This is fully consistent with the collapse of $-\overline{u_1 u_2}^*$ in three wall flows when $Re_\tau > 1000$, up to $x_2^* = 40$ (see figure 10d). Note that $x_2^* = 40$ corresponds to $x_2^+ = 103$ at $Re_\tau = 10^4$. In contrast, the variation in the channel of $-\overline{u_1 u_2}^+$ for $Re_\tau > 1000$ and $x_2^+ \lesssim 103$ is systematic (see figure 26b). The present scaling is superior to that based on wall parameters in the context of (B1) and (B2) over the present Re_τ range. It is worth mentioning that (2.1) can be generalized to the scale-by-scale energy equation, or equivalently the transport equation for the second-order velocity structure function (see, for example, (2.23) of Danaila *et al.* (2001), or (3.4) of Marati, Casciola & Piva 2004). Applying the limit at scale $\to \infty$ to the scale-by-scale energy equation yields the transport equation for $\overline{u_i u_i}$, i.e. (2.1). The scale-by-scale energy equation describes the relative importance of the energy production, energy transfer and dissipation in different regions of the flow and for different ranges of scales; it also highlights the importance of the local value of $\bar{\varepsilon}$ in the context of the present scaling. Based on our analysis in the context of (2.1), it can be expected that as $Re_\tau \to \infty$, all the terms in the scale-by-scale energy equation, after normalizing by $\bar{\varepsilon}$ and ν, in the range $x_2^* \ll \delta^*$ at all scales, should be independent of Re_τ, which leads to the Re_τ independence of processes involved in the energy production, energy transfer and energy dissipation in wall flows. This expectation is consistent with our prediction summarized in figure 22, and merits further investigation.
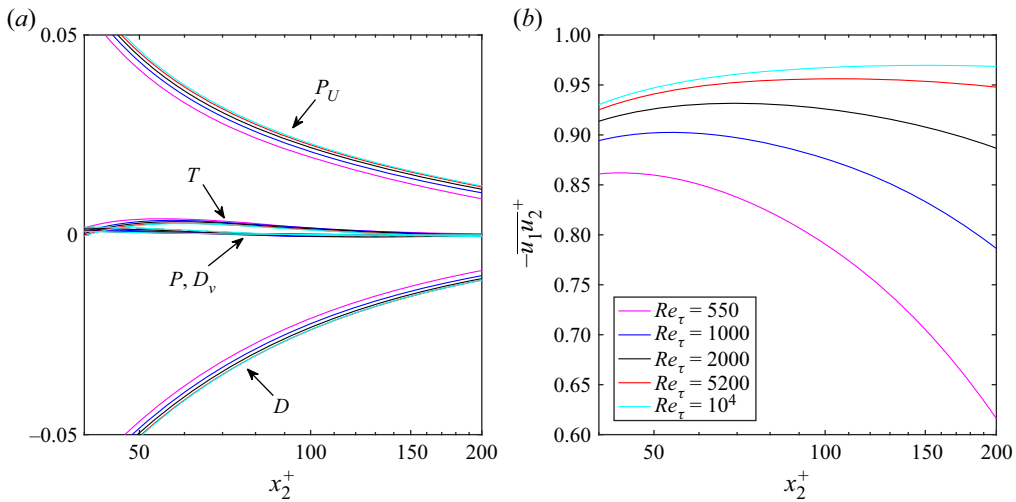
Figure 26. (*a*) Distributions of terms in (2.1), normalized by wall parameters, in a channel. (*b*) Distributions of $-\overline{u_1 u_2}^+$ in a channel. Data of Lee & Moser (2015, 2019), Alcántara-Ávila *et al.* (2021) and Hoyas *et al.* (2022).

REFERENCES

ABE, H., ANTONIA, R.A. & KAWAMURA, H. 2009 Correlation between small-scale velocity and scalar fluctuations in a turbulent channel flow. *J. Fluid Mech.* **627**, 1–32.

ALCÁNTARA-ÁVILA, F. & HOYAS, S. 2021 Direct numerical simulation of thermal channel flow for medium-high Prandtl numbers up to $Re_\tau = 2000$. *Int. J. Heat Mass Transfer* **176**, 121412.

ALCÁNTARA-ÁVILA, F., HOYAS, S. & PÉREZ-QUILES, M.J. 2018 DNS of thermal channel flow up to $Re_\tau = 2000$ for medium to low Prandtl numbers. *Int. J. Heat Mass Transfer* **127**, 349–361.

ALCÁNTARA-ÁVILA, F., HOYAS, S. & PÉREZ-QUILES, M.J. 2021 Direct numerical simulation of thermal channel flow for $Re_\tau = 5000$ and $Pr = 0.71$. *J. Fluid Mech.* **916**, A29.

ANTONIA, R.A., ABE, H. & KAWAMURA, H. 2009 Analogy between velocity and scalar fields in a turbulent channel flow. *J. Fluid Mech.* **628**, 241–268.

ANTONIA, R.A. & KIM, J. 1994 Low-Reynolds-number effects on near-wall turbulence. *J. Fluid Mech.* **276**, 61–80.

BAILEY, S.C.C., KUNKEL, G.J, HULTMARK, M., VALLIKIVI, M., HILL, J.P., MEYER, K.A., TSAY, C., ARNOLD, C.B. & SMITS, A.J. 2010 Turbulence measurements using a nanoscale thermal anemometry probe. *J. Fluid Mech.* **663**, 160–179.

BERNARDINI, M., PIROZZOLI, S. & ORLANDI, P. 2014 Velocity statistics in turbulent channel flow up to $Re_\tau = 4000$. *J. Fluid Mech.* **742**, 171–191.

BORRELL, G., SILLERO, J.A. & JIMÉNEZ, J. 2013 A code for direct numerical simulation of turbulent boundary layers at high Reynolds numbers in BG/P supercomputers. *Comput. Fluids* **80**, 37–43.

CHEN, X. & SREENIVASAN, K.R. 2021 Reynolds number scaling of the peak turbulence intensity in wall flows. *J. Fluid Mech.* **908**, R3.

CHEN, X. & SREENIVASAN, K.R. 2022 Law of bounded dissipation and its consequences in turbulent wall flows. *J. Fluid Mech.* **933**, A20.

DANAILA, L., ANSELMET, F., ZHOU, T. & ANTONIA, R.A. 2001 Turbulent energy scale-budget equations in a fully developed channel flow. *J. Fluid Mech.* **430**, 87–109.

DICKEY, T.D. & MELLOR, G.L. 1979 The Kolmogoroff $r^2/3$ law. *Phys. Fluids* **22**, 1029–1032.

FULACHIER, L. & ANTONIA, R.A. 1983 Turbulent Reynolds and Péclet numbers re-defined. *Int. Commun. Heat Mass Transfer* **10** (5), 435–439.

FULACHIER, L. & ANTONIA, R.A. 1984 Spectral analogy between temperature and velocity fluctuations in several turbulent flows. *Intl J. Heat Mass Transfer* **27** (7), 987–997.

FULACHIER, L. & DUMAS, R. 1976 Spectral analogy between temperature and velocity fluctuations in a turbulent boundary layer. *J. Fluid Mech.* **77** (2), 257–277.

Hoyas, S., Oberlack, M., Alcántara-Ávila, F., Kraheberger, S.V. & Laux, J. 2022 Wall turbulence at high friction Reynolds numbers. *Phys. Rev. Fluids* **7**, 014602.

Hultmark, M., Vallikivi, M., Bailey, S.C.C. & Smits, A.J. 2012 Turbulent pipe flow at extreme Reynolds numbers. *Phys. Rev. Lett.* **108**, 094501.

Hultmark, M., Vallikivi, M., Bailey, S.C.C. & Smits, A.J. 2013 Logarithmic scaling of turbulence in smooth- and rough-wall pipe flow. *J. Fluid Mech.* **728**, 376–395.

Jiménez, J., Hoyas, S., Simens, M.P. & Mizuno, Y. 2010 Turbulent boundary layers and channels at moderate Reynolds numbers. *J. Fluid Mech.* **657**, 335–360.

Kaneda, Y. & Yamamoto, Y. 2021 Velocity gradient statistics in turbulent shear flow: an extension of Kolmogorov's local equilibrium theory. *J. Fluid Mech.* **929**, A13.

Kolmogorov, A.N. 1941 Local structure of turbulence in an incompressible fluid for very large Reynolds numbers. *Dokl. Akad. Nauk SSSR* **30**, 299–303.

Kunkel, G., Arnold, C.B. & Smits, A.J. 2006 Development of NSTAP: nanoscale thermal anemometry probe. *AIAA Paper* 2006-3718.

Lee, M. & Moser, R.D. 2015 Direct numerical simulation of turbulent channel flow up to $Re_\tau = 5200$. *J. Fluid Mech.* **774**, 395–415.

Lee, M. & Moser, R.D. 2019 Spectral analysis of the budget equation in turbulent channel flows at high Reynolds number. *J. Fluid Mech.* **860**, 886–938.

Lluesma-Rodríguez, F., Hoyas, S. & Perez-Quiles, M.J. 2018 Influence of the computational domain on DNS of turbulent heat transfer up to $Re_\tau = 2000$ for $Pr = 0.71$. *Int. J. Heat Mass Transfer* **122**, 983–992.

Marati, N., Casciola, C.M. & Piva, R. 2004 Energy cascade and spatial fluxes in wall turbulence. *J. Fluid Mech.* **521**, 191–215.

Marusic, I., Baars, W.J. & Hutchins, N. 2017 Scaling of the streamwise turbulence intensity in the context of inner–outer interactions in wall turbulence. *Phys. Rev. Fluids* **2**, 100502.

Marusic, I., McKeon, B.J., Monkewitz, P.A., Nagib, H.M., Smits, A.J. & Sreenivasan, K.R. 2010 Wall-bounded turbulent flows at high Reynolds numbers: recent advances and key issues. *Phys. Fluids* **22**, 065103.

Marusic, I. & Monty, J.P. 2019 Attached eddy model of wall turbulence. *Annu. Rev. Fluid Mech.* **51**, 49–74.

Monin, A.S. & Yaglom, A.M. 2007 *Statistical Fluid Dynamics*, vol. 2. MIT.

Monty, J.P., Hutchins, N., Ng, H.C.H., Marusic, I. & Chong, M.S. 2009 A comparison of turbulent pipe, channel and boundary layer flows. *J. Fluid Mech.* **632**, 431–442.

Perry, A.E., Henbest, S. & Chong, M.S. 1986 A theoretical and experimental study of wall turbulence. *J. Fluid Mech.* **165**, 163–199.

Pirozzoli, S., Romero, J., Fatica, M., Verzicco, R. & Orlandi, P. 2021 One-point statistics for turbulent pipe flow up to $Re_\tau \approx 6000$. *J. Fluid Mech.* **926**, A28.

Pirozzoli, S., Romero, J., Fatica, M., Verzicco, R. & Orlandi, P. 2022 DNS of passive scalars in turbulent pipe flow. *J. Fluid Mech.* **940**, A45.

Pope, S.B. 2000 *Turbulent Flows*. Cambridge University Press.

Rosenberg, B.J., Hultmark, M., Vallikivi, M., Bailey, S.C.C. & Smits, A.J. 2013 Turbulence spectra in smooth- and rough-wall pipe flow at extreme Reynolds numbers. *J. Fluid Mech.* **731**, 46–63.

Samie, M., Marusic, I., Hutchins, N., Fu, M.K., Fan, Y., Hultmark, M. & Smits, A.J. 2018 Fully resolved measurements of turbulent boundary layer flows up to $Re_\tau = 20\,000$. *J. Fluid Mech.* **851**, 391–415.

Sillero, J.A., Jiménez, J. & Moser, R.D. 2013 One-point statistics for turbulent wall-bounded flows at Reynolds numbers up to $\delta^+ \approx 2000$. *Phys. Fluids* **25**, 105102.

Simens, M.P., Jiménez, J., Hoyas, S. & Mizuno, Y. 2009 A high-resolution code for turbulent boundary layers. *J. Comput. Phys.* **228**, 4218–4231.

Smits, A.J. 2022 Batchelor prize lecture: measurements in wall-bounded turbulence. *J. Fluid Mech.* **940**, A1.

Smits, A.J., Hultmark, M., Lee, M., Pirozzoli, S. & Wu, X. 2021 Reynolds stress scaling in the near-wall region of wall-bounded flows. *J. Fluid Mech.* **926**, A31.

Smits, A.J, McKeon, B.J. & Marusic, I. 2011*b* High-Reynolds number wall turbulence. *Ann. Rev. Fluid Mech.* **43**, 353–375.

Smits, A.J., Monty, J., Hultmark, M., Bailey, S.C.C., Hutchins, N. & Marusic, I. 2011*a* Spatial resolution correction for wall-bounded turbulence measurements. *J. Fluid Mech.* **676**, 41–53.

Tang, S.L. & Antonia, R.A. 2022 Scaling of small-scale wall turbulence. *J. Fluid Mech.* **948**, A25.

Townsend, A.A. 1976 *The Structure of Turbulent Shear Flow*, vol. 2. Cambridge University Press.

Vallikivi, M., Ganapathisubramani, B. & Smits, A.J 2015*a* Spectral scaling in boundary layers and pipes at very high Reynolds numbers. *J. Fluid Mech.* **771**, 303–326.

VALLIKIVI, M., HULTMARK, M., BAILEY, S.C.C. & SMITS, A.J. 2011 Turbulence measurements in pipe flow using a nano-scale thermal anemometry probe. *Exp. Fluids* **51**, 1521–1527.

VALLIKIVI, M., HULTMARK, M. & SMITS, A.J. 2015*b* Turbulent boundary layer statistics at very high Reynolds number. *J. Fluid Mech.* **779**, 371–389.

VALLIKIVI, M. & SMITS, A.J 2014 Fabrication and characterization of a novel nanoscale thermal anemometry probe. *J. Microelectromech. Syst.* **23**, 899–907.

VINCENTI, P., KLEWICKI, J., MORRILL-WINTER, C., WHITE, C.M. & WOSNIK, M. 2013 Streamwise velocity statistics in turbulent boundary layers that spatially develop to high Reynolds number. *Exp. Fluids* **54**, 1–13.

WILLERT, C.E., SORIA, J., STANISLAS, M., KLINNER, J., AMILI, O., EISFELDER, M., CUVIER, C., BELLANI, G., FIORINI, T. & TALAMELLI, A. 2017 Near-wall statistics of a turbulent pipe flow at shear Reynolds numbers up to 40 000. *J. Fluid Mech.* **826**, R5.